2-3-2022

Venus Mountain Waves in the Upper Atmosphere Simulated by A Time-Invariant Linear Full-Wave Spectral Model

Michael P. HIckey
Embry-Riddle Aeronautical University, hicke0b5@erau.edu

Richard L. Walterscheid
Embry-Riddle Aeronautical University, walter10@erau.edu

Thomas Navarro
Embry-Riddle Aeronautical University

Gerald Schubert
Embry-Riddle Aeronautical University

Icarus 377 (2022) 114922

Contents lists available at ScienceDirect

Icarus

journal homepage: www.elsevier.com/locate/icarus

Venus mountain waves in the upper atmosphere simulated by a time-invariant linear full-wave spectral model

Michael P. Hickey [a,b,*], Thomas Navarro [c], Gerald Schubert [c], Richard L. Walterscheid [b]

[a] Department of Physical Sciences, Embry-Riddle Aeronautical University, Daytona Beach, FL, USA
[b] Center for Space and Atmospheric Research, Embry-Riddle Aeronautical University, Daytona Beach, FL, USA
[c] Department of Earth, Planetary and Space Sciences, UCLA, CA, USA

ARTICLE INFO

Keywords:
Venus atmosphere
Venus surface
Atmospheric dynamics
Atmospheric structure
Aeronomy

ABSTRACT

A 2-D spectral full-wave model is described that simulates the generation and propagation of mountain waves over idealized topography in Venus' atmosphere. Modeled temperature perturbations are compared with the Akatsuki observations. Lower atmosphere eddy diffusivity and stability play a major role in the upward propagation of gravity waves from their mountain sources. Two local times (LT) are considered. For LT = 11 h the waves are blocked by a critical level near 100 km altitude, while for LT = 16 h the waves propagate into the thermosphere. As a result of the small scale height in the Venus thermosphere, for LT = 16 h wave amplitudes grow with increasing altitude up to ~200 km, despite the increasing kinematic viscosity. Although wave amplitudes can become very large in the thermosphere, the value of the total potential temperature gradient suggests that some of these fast waves having extremely large vertical wavelengths may remain convectively stable. Our simulations suggest that the momentum and thermal forcing of the mean state due to the dissipating waves may, at times, be extremely large in the thermosphere. At a given local time, the maximum forcing of the mean state always occurs at an altitude determined by the mean winds and the upper atmospheric viscosity. The surface conditions that determine the forcing (mountain parameters, surface mean wind, eddy diffusivity, and static stability) have little impact on this altitude, but they do significantly impact the magnitude of the forcing.

1. Introduction

1.1. Observations

Observations made from the Akatsuki satellite of large stationary features at the cloud tops in the upper atmosphere of Venus were first identified by Fukuhara et al. (2017). These observations were made on the dayside of Venus using the Longwave Infrared Camera (which has a spectral band of 8 to 12 μm) and the Ultraviolet Imager. The former images UV radiation scatter by cloud particles at the cloud tops (near 65 km altitude) while the latter detects thermal radiation from the same region. The features extended some 10,000 km of latitude, were stationary with respect to underlying surface topography, found above highlands, bow-shaped, and were thus tentatively identified as gravity waves. This discovery challenged the previously established view of a fast, superrotating cloud deck circulation minimally impacted by the slowly rotating surface circulation. The brightness-weighted temperature was determined to be up to about 2 K and centered at ~65 km altitude with a full-width at half-maximum of ~10 km. Kitahara et al. (2019) and Kouyama et al. (2017) found that bow-shaped stationary wave features occurred exclusively above highlands and tended to appear between noon and evening. Specifically, Kouyama et al. (2017) examined the local time dependence of stationary waves in four different highland regions, and found that stationary waves were in every region for local times of 15–16 h. They also noted that the waves were not completely stationary, but instead migrated slowly by as much as 20° eastward (the upstream direction) over a period of ~10.5 Earth days. Smaller scale stationary waves that are not bow-shaped have also been observed in the upper cloud regions of Venus's night-side atmosphere that appear to be correlated with highland regions (Peralta et al., 2017). The stationary wave features observed in the UV emissions at the cloud tops by Kitahara et al. (2019) had a horizontal wavelength of ~510 km and a radiance amplitude of ~1.2%. They hypothesized that "the waves should reach thermospheric heights and decay via molecular

* Corresponding author at: Department of Physical Sciences and Center for Space and Atmospheric Research, Embry-Riddle Aeronautical University, Daytona Beach, FL 32114, USA.
E-mail address: hicke0b5@erau.edu (M.P. Hickey).

https://doi.org/10.1016/j.icarus.2022.114922
Received 17 August 2021; Received in revised form 22 January 2022; Accepted 31 January 2022
Available online 3 February 2022

viscosity on the dusk side where the westward superrotation extends to the thermosphere, while the waves will decay via radiative damping or critical layer absorption on the dawn side where the superrotation vanishes at high altitudes." They also stressed the need for further measurements of topographic gravity waves in order to infer properties of the surface boundary layer, because measured wave parameters at the cloud tops could provide constraints on static stability and wind speed near the surface where the waves are generated.

1.2. Earlier modeling

Schubert and Walterscheid (1984) used a full-wave model to examine the propagation and dissipation of gravity waves in a zonal-mean flow that were forced at the surface in the Venus atmosphere. Both a very low static stability and a more stable static stability in the near-surface atmosphere were considered. They found that the vertical transmission of wave energy from the surface depends crucially on gravity wave intrinsic phase speed. Because slow waves propagating in a more stable atmosphere have smaller vertical wavelengths, they were strongly attenuated by eddy diffusion. Fast waves which were strongly evanescent in regions of low static stability were also strongly attenuated. Slow in this context means slow enough in terms of intrinsic frequency (or phase speed) to produce waves that are rapidly dissipated by scale-dependent diffusion.

Young et al. (1987) used the model of Schubert and Walterscheid (1984) to simulate the wave response near 54 km altitude due to waves generated near the surface. Their study was motivated by an apparent correlation of vertical wind amplitude with the mountainous region Aphrodite Terra, as observed by a VEGA balloon (Blamont et al., 1986). These simulations were used to help explain the VEGA Venus Balloon Mission measurements, which revealed enhanced vertical wind amplitudes of 2–3 m/s at ~55 km altitude over Aphrodite Terra, and apparent zonal wavelengths of ~500 km. In particular, the power spectra of topology, which determines the spectrum of the forced waves indicated that terrain-forced gravity waves could explain a significant portion of the VEGA balloon measurements above Aphrodite Terra. The study of Young et al. (1987) was extended by Young et al. (1994) using the numerical gravity wave model of Walterscheid and Schubert (1990). It was demonstrated that although small scale waves cannot propagate to high altitudes (near the cloud level at ~55 km), nonlinear wave-wave interactions would generate smaller scale waves at these altitudes, resulting in complex flow patterns. Additionally, it was shown that the vertical structure of the mean wind and temperature can lead to partial wave trapping and resonances of upward propagating stationary waves, with the result that wave amplitudes at cloud levels depended on the magnitude of the surface wind in a nonmonotonic way.

1.3. Recent numerical simulations

Navarro et al. (2018) used the Institut Pierre-Simon Laplace (IPSL) general circulation model to demonstrate that the observations of large stationary features at the cloud tops were consistent with mountain waves. They also showed that the diurnal cycle of near-surface atmospheric stability and near-surface winds favored the afternoon generation and propagation of these waves. They furthermore demonstrated that the mountain waves would generate a substantial atmospheric torque that could impact the planetary rotation rate.

Yamada et al. (2019) hypothesized that the prevalence of stationary waves just above the cloud top in the afternoon might be related to the afternoon thinning of the region of low static stability in the 50–60 km altitude region. They reasoned that gravity waves should be strongly attenuated when propagating through this region of evanescence at other times, when it is thicker. However, the results of their modeling demonstrated that stationary gravity waves with zonal wavelengths longer than 1000 km can propagate to the cloud top, even for a deep (~15 km) region of low static stability. They concluded that the observed dependence of mountain wave amplitudes on local time must be due to a corresponding time dependence of the excitation process of the waves and/or transmission process in the lower atmosphere.

Lefèvre et al. (2020) used a mesoscale model to perform a detailed study of mountain wave propagation. They found that the two regions of low static stability (lying between altitudes of 18 and 35 km, and 48 and 52 km, respectively) supported trapped lee waves that propagate horizontally. They also found that in spite of the existence of these low-stability barriers to wave propagation, the energy transmission via tunneling was sufficient to allow significant wave propagation to the Venus cloud tops. The bow-shape waves resolved by their IPSL Venus mesoscale model achieved maximum amplitudes of ~2 K near the cloud tops in the late afternoon, but these had decreased to less than 0.5 K by midnight. They noted that the near surface winds responsible for orographic wave generation had not changed significantly during the day and concluded that the diurnal variability of atmospheric conditions (atmospheric stability) at higher altitudes (the first 4 or 5 km) were more likely to explain the diurnal variation of the bow-shaped waves. Lefèvre et al. (2020) also calculated the mean state acceleration due to the divergence of the wave momentum flux and found that the mean winds were decelerated by about 3 m/s over the course of a Venus day. It was noted that this value was smaller than that required to explain the longitudinal shift of zonal wind patterns previously inferred by Bertaux et al. (2016).

In this paper we examine the propagation of stationary gravity waves forced at the Venus surface using a time-independent linear spectral full-wave model. The primary objective is to determine how these waves force the mean state at high altitudes (upper troposphere and thermosphere). In order to do so we: a) determine the dependence of the wave generation on near surface winds, local time, lower atmosphere stability and eddy diffusivity, and b) determine the wave-driven transport (fluxes) of heat and momentum to the upper troposphere and thermosphere and their flux divergences to assess the wave forcing of the high-altitude mean state. Our study focusses on zonal mean-state effects on the propagation of waves excited by flow over idealized topography. We examine the basic effects of the diurnal variation of wind and thermal structure on the propagation and dissipation of waves in different parts of the wave spectrum. We do not address the effects of perturbed background states, including the effects of zonal variations in the background flow that may be significant episodically or regionally.

Section 2 presents basic mountain wave theory, section 3 describes the numerical model, and section 4 describes the mean state specification. Results are presented in section 5, a discussion is provided in section 6 and conclusions are provided in section 7.

2. Mountain wave theory

Excellent introductory texts on mountain wave theory are provided by Smith (1980) and Durran (2003) and references therein. Based on Boussinesq flow, the so-called Scorer parameter, l_s, is defined by $l_s^2 = \frac{N^2}{\overline{U}^2} - \frac{1}{\overline{U}}\frac{d^2\overline{U}}{dz^2}$, where $\overline{U}$ is the mean zonal wind, and N is the Brunt-Väisälä (buoyancy) frequency. A simplified dispersion relation for atmospheric gravity waves is $m^2 = l_s^2 - k^2$, where k and m are the horizontal and vertical wavenumbers, respectively. The Scorer parameter therefore represents the maximum vertical wavenumber (minimum vertical wavelength) for propagating waves. For waves with $l_s^2 > k^2$ the waves propagate vertically without loss of amplitude and the wave crests tilt upstream with increasing height, but the waves are evanescent for $l_s^2 < k^2$ (Durran, 2003).

For mountains having a large characteristic width a, the generated waves will be approximately hydrostatic when $Na/\overline{U} \gg 1$ and will be confined to a region directly above the mountain. Under such conditions the characteristic time for the wind to traverse the mountain will be considerably longer than the Brunt-Väisälä period. Non-hydrostatic

gravity waves will be created for narrow mountains satisfying $Na/\overline{U} \ll 1$, and downstream disturbances are then possible when $\overline{U}$ and N vary appreciably with height.

The parameter $\overline{U}/Nh_0$, which is the Froude (Fr) number, and where h_0 is the mountain height, is a measure of wave nonlinearity (e. g. Smith, 1980; Young et al., 1994). Typically, linear theory breaks down with the onset of blocking, which occurs when $\overline{U}/Nh_0 \approx 1$ (the critical Froude number). When $Fr > 1$ the motion is linear and longer wavelength waves are produced. When $Fr << 1$, the motion is nonlinear, and some flow occurs over the mountain top. In this case lateral flow will occur around an isolated mountain at low altitudes, but blocking will occur if the mountain(s) are wide. When $Fr = 1$, a resonance may occur, leading to intense mountain waves. These situations have been well described by Durran (1990). For our simulations, the mountain height was set a value of 1.0 km, which is reasonable for most conditions considered. A more detailed appraisal of this assumption is provided in the discussion section. Under these circumstances hydrostatic gravity waves will occur for $a \gg (h_0)_{max}$(small mountain slope) and non-hydrostatic gravity waves will occur for $a \ll (h_0)_{max}$(large mountain slope), where a is a mountain width parameter. Finally, we remark that as Young et al. (1994) stated, waves that are close to overturning in limited regions at low levels will not be close to overturning at higher altitudes away from the lower boundary because the mean wind increases with increasing height.

3. Mountain wave model

We use a high-resolution, compressible, spectral model to simulate mountain gravity waves in the Venus atmosphere. Spectral models have been previously employed to model mountain wave propagation in the terrestrial atmosphere (Eckermann et al., 2016, and references therein). The main difference between our model and previous spectral models is that ours is based on a full-wave model while the previous models were based on the WKB approximation. Our model accounts for wave reflection, while WKB models do not. The topic of wave reflection in the Venus atmosphere has been addressed by Young et al. (1994).

Our model is based on a single-gas full-wave model that solves the linearized Navier-Stokes equations subject to boundary conditions for a non-isothermal mean-state atmosphere including the effects of height-dependent mean winds, and the eddy and molecular diffusion of energy and momentum. It can model the transmission and reflection of gravity waves associated with regions of quasi-evanescence, which is important to consider for wave propagation in regions of low static stability in the Venus atmosphere (Schubert and Walterscheid, 1984). A detailed description of the full-wave model and equations are provided in Appendix A.

Spectral versions of this model have been used previously to study the effect of time-dependent gravity wave packets on atomic oxygen transport in Earth's mesosphere (Hickey et al., 2000b) and the effect of tsunami-driven wave packets on the terrestrial ionosphere (Hickey et al., 2009). We use a similar approach based on discrete Fourier transforms of wave variables. We present the equations appropriate to a 1-D mountain shape in the x-z plane. If a mean wind $\overline{U}(z)$ blows across a mountain with terrain $h(x)$, the vertical velocity at the lower boundary will be

$$w(x,0) = \overline{U}\,\partial h(x)/\partial x \tag{1}$$

With the terrain represented as

$$h(x) = \frac{1}{2\pi}\int_{-\infty}^{\infty} \widehat{h}(k)\, e^{-ikx}\, dk \tag{2}$$

Eq. (1) gives the vertical velocity spectrum at the lower boundary:

$$\widehat{w}\,(k,0) = -ik\overline{U}\,\widehat{h}(k) \tag{3}$$

The full-wave model provides solutions $\widehat{\psi}_j(k,z)$ where the subscript j corresponds to perturbations in one of the dependent variables: the x-z velocity components u', w', respectively, temperature T' and pressure p'. The total wave response to the forcing is written as

$$\psi_j'(x,z) = \frac{1}{2\pi}\int_{-\infty}^{\infty} \widehat{h}(k)\widehat{\psi}_j(k,z)\, e^{-ikx}\, dk \tag{4}$$

subject to specification of the vertical velocity at the lower boundary using Eq. (3). The implementation is by means of discrete Fourier transforms. We found by experimentation that for our 2-D simulations in one horizontal coordinate, 1000 individual waves with a horizontal grid spacing equivalent to $0.1a$ (see Eq. (5)) provided convergent results. Increasing the number of waves in the spectrum to 2000 had virtually no impact on the results.

For our 2-D simulations we assume a mountain shape based on that of Reinecke and Durran (2009) which in the x-z plane is defined by:

$$\begin{aligned} h(x) &= \frac{h_0}{16}\left[1 + cos\left(\frac{\pi x}{4a}\right)\right]^4 \quad if|x/4a| \le 1 \\ &= 0 \quad \text{otherwise} \end{aligned} \tag{5}$$

For an assumed 1-D mountain shape the discrete Fourier transform is used to derive the spectrum $\widehat{h}(k)$(not shown), and with the prescribed mean wind at the lower boundary we calculate $\widehat{w}(k,0)$. For most of our simulations we use a value of $a = 100$ km and $h_0 = 1000$ m in Eq. (5). The resulting mountain shape is shown in Fig. 1.

Observations and numerical studies indicate that linear theory reliably predicts the amplitude of trapped lee waves generated by finite-amplitude mountains, the main shortcomings of linear theory being that it does not represent the tendency of nonlinear dynamics to enhance the short-wavelength Fourier components in the low-level wave field over the lee slope (*Durran*, 2015). The nonlinear behavior induced by blocking should not propagate to heights well above the terrain (Young et al., 1994). Thus, linear theory should give reasonably accurate descriptions of the gross behavior of bow waves. Further, the low static stability at terrain altitudes will mitigate the effects of nonlinearities induced by the terrain. Temperature data below ~30 km are sparse, but the available data and modeling indicate that lapse rates are indicative of near neutral stability indicating that blocking should not occur except for the highest terrain (*Seiff* et al., 1980; *Lewis*, 2004; *Lebonnois and Schubert*, 2017; Navarro et al., 2018).

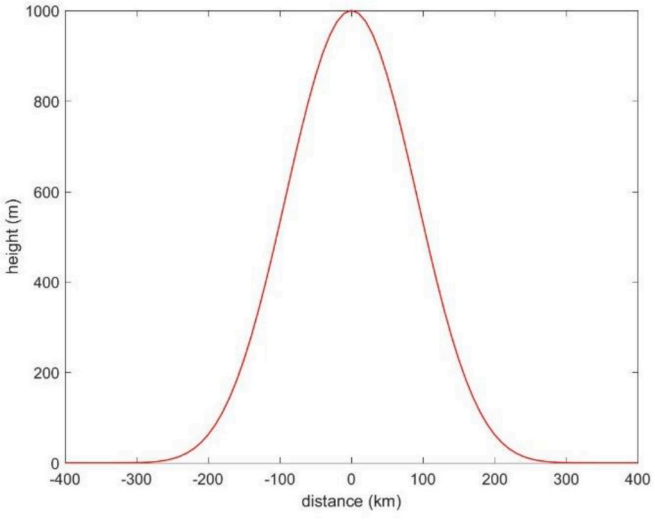

Fig. 1. 1-D mountain shape for $a = 100$ km and $h_0 = 1000$ m in Eq. (5).

4. Mean state definition

Our model is based on the propagation of linear waves in an otherwise undisturbed, steady background atmosphere. The assumption that the mean state does not vary in time is reasonable for the waves that we consider here. For the assumed background atmospheric parameters, and for a representative horizontal wavelength of 500 km, we estimate that an average vertical group speed is approximately 2.5 m/s between the surface and 100 km altitude. This means that the waves will traverse that region in a time of order 10 h. This propagation time is exceedingly small compared to the slow rotation rate of Venus, supporting our assumption of a steady mean state. At altitudes higher than 100 km we expect the waves will either propagate at a speed much greater than 2.5 m/s in one case considered, or not propagate at all in the other case (see further discussion of this latter situation later in this section).

The mean state used in the simulations is provided from the IPSL ground-to-thermosphere GCM simulations at an increased horizontal resolution of 96 × 96 (Navarro et al., 2021; Gilli et al., 2021). These profiles, averaged on low-latitude (10^oS-10^oN) conditions and over one solar day, are smoothed, and extended to higher altitudes using cubic splines and polynomials that ensure that gradients of key parameters (e.g., temperature, winds) smoothly approach zero near the upper boundary. The cubic spline fitting enables us to map the IPSL profiles to the high resolution full-wave model grid. Smoothing tends to minimize any artificial reflections that may occur in the full-wave model. Contrary to the GCM assumptions, we assume that the ideal gas equation of state applies throughout the atmosphere. Although this assumption will break down in the deep atmosphere of Venus, Lebonnois and Schubert (2017) have shown that the error associated with this assumption does not exceed ~0.8%. All species mixing ratios are specified by the IPSL model. The molecular viscosity is provided by the IPSL model, while the thermal conductivity for each species was calculated from *Rees* (1989) for O, O_2 and N_2, and from Huber and Harvey (2011) for the remaining species (CO, CO_2, SO_2 and H_2O).

In this study we select atmospheric profiles for two local times, one set of profiles representing morning conditions and the other representing afternoon conditions. Because the propagation of mountain waves is primarily sensitive to the mean winds through which they propagate, the two local times we selected for our simulations were based solely on the mean zonal wind profiles. Daytime profiles of these hourly winds derived from the IPSL GCM model for local times of 09 LT to 18 LT (not shown) were examined. For every local time between 09 h and 14 h (inclusive) a critical level for mountain waves (where $\overline{U} = 0$) was seen to exist near 100 km altitude. Such critical levels severely impede the propagation of the waves into the thermosphere (the waves cannot propagate above about 100 km altitude). Because the winds below about 100 km were similar for these local times, a local time of 11 h was selected as representative of morning conditions. For local times between 15 h and 18 h (inclusive) it was noted that no critical levels existed anywhere, while above about 100 km altitude the winds increased dramatically in the westward direction and achieved large values above about 120 km altitude. The largest westward wind at 150 km altitude was ~214 m/s and occurred for LT = 16 h. This profile was chosen to represent afternoon conditions.

The mean zonal wind in the lowest region of the atmosphere (z < 7 km) is assumed to be approximately constant, but we also investigate the effects of a small non-zero vertical shear at the lower boundary. The value of the surface wind is adjustable, and values between 1 m/s and 5 m/s (westward) are considered in our simulations. Pioneer Venus Sounder (PVS) mean winds were used for altitudes between about 15 km and 59 km and IPSL GCM model winds were used from about 65 km to 150 km altitude. For altitudes above 150 km the winds were extrapolated upward using a polynomial that provided a zero gradient at high altitudes. In the region between ~7 km and 15 km altitude the winds were defined by a 4th degree polynomial, while those between ~59 km and 65 km altitude were based on a fairing that smoothly joined the PVS winds to the IPSL GCM model winds.

The wind profiles for LT = 11 h and LT = 16 h are shown in Fig. 2. Below about 68 km altitude the winds for the two local times, although not identical, exhibit similar behavior in a region where the circulation is dominated by the westward superrotation, but they diverge significantly at higher altitudes where the subsolar-to-antisolar circulation prevails. For LT = 11 h the winds become increasingly westward with increasing altitude up to about 68 km altitude, and then remain approximately constant up to about 86 km altitude. Above that altitude the winds rapidly decrease in magnitude, becoming eastward above about 102 km altitude. The wind continues to increase in magnitude at greater heights, and eventually asymptotes to an eastward speed of about 67 m/s. For LT = 16 h the winds increase (westward) with increasing altitude up to about 73 km altitude and then decrease in magnitude to a local minimum of about 72 m/s slightly above 100 km altitude. At greater heights, the wind increases in the westward direction, and eventually asymptotes to a value of about 215 m/s at high altitudes. We assume the dayside SS-AS flow speeds at high altitudes are constant, as modeled and explained with a GCM in Navarro et al. (2021).

The nominal temperature profile we used was constructed by smoothly joining several regions. For each local time, two different temperature profiles were considered. The first represents a nominal profile, in which the region between 5 km and 150 km altitude is defined by a nominal IPSL GCM temperature profile. This profile is smoothed, and then extended to higher altitudes using a polynomial that provides an isothermal atmosphere above ~200 km altitude. The temperature in the lowest 5 km of the atmosphere is based on a polynomial that smoothly joins to the IPSL LMD profile at 5 km altitude and that becomes isothermal as the lower boundary is approached.

The second temperature profile is based on the low stability low-altitude profiles derived from the IPSL GCM and differs from the nominal profile only for altitudes below about 60 km. A cubic polynomial is used to provide a fit to an N^2 profile between the surface and 35 km altitude. This requires continuity of both N^2 and dN^2/dz with the existing N^2 profile at ~35 km altitude, while N^2 is set to the low-stability value of N^2 at the surface with dN^2/dz set equal to zero. From this new N^2 profile, the modified temperature profile is determined as follows. Starting with the definition of N^2 based on the potential temperature gradient ($N^2 = g\frac{d\ln\theta}{dz}$), a finite difference equation is derived for the temperature: $T_{n-1} =$

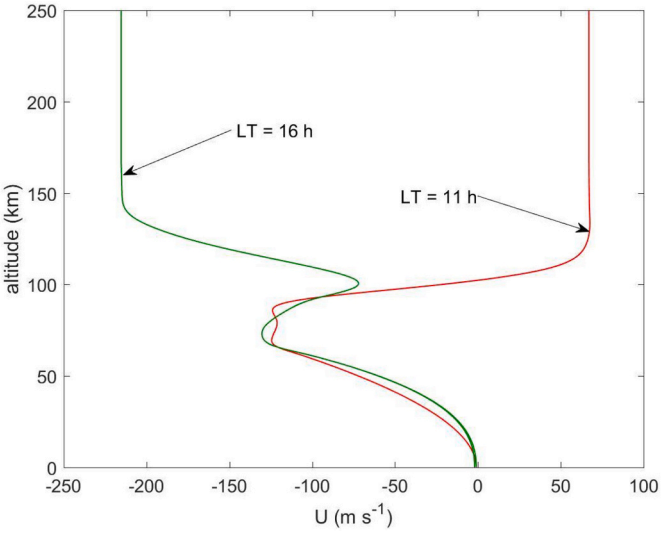

Fig. 2. Mean zonal winds for LT = 11 h (red curve) and LT = 16 h (green curve). The nominal winds shown here have a lower boundary value of −2 ms^{-1}. Positive corresponds to the eastward direction. (For interpretation of the references to colour in this figure legend, the reader is referred to the web version of this article.)

$T_{n+1} - \frac{2hN_n^2}{g_n}T_n + \frac{2h}{R}g_n M_n \kappa_n$, where the step size is h, $\kappa = R/c_p$and all other variables are as defined in Appendix A. Here, T refers to temperature and the subscript "n" refers to the position on the altitude grid. Starting from the upper height of the modified profile (~ 35 km) where all values on the right side of the equation are defined, we proceed downward to the surface. In general, this won't provide the required surface temperature, T_1, but by adding a constant we can achieve the required surface temperature without affecting the N^2 profile. However, the added constant will affect the continuity of the temperature near 35 km altitude requiring a final adjustment. This is achieved using a 5th-degree polynomial to smoothly join the temperature between altitudes of 35 km (the new lower atmosphere temperature profile) and 60 km (the initial temperature profile). This polynomial was based on the continuity of the temperature and its first and second derivatives at the two endpoints.

The temperature profiles for two local times (11 h and 16 h) are shown in the left panel of Fig. 3 for nominal conditions (solid curves) and low stability conditions (dashed curves). The dependence of the nominal temperature on local time is not large and becomes noticeable only above ~80 km altitude. At high altitudes, the temperature asymptotes to ~213 K and 205 K for LT = 11 h and 16 h, respectively. At the lower boundary, the temperature is 700 K. The low stability profiles below 60 km altitude are similar for the two local times and exhibit larger negative gradients than those of the nominal temperature profiles.

The right panel of Fig. 3 shows the square of the Brunt-Väisälä frequency (N^2) for the two local times and for nominal and low stability conditions. For the nominal-stability lower atmosphere, the lower boundary value of N^2 is ~1.25×10^{-4} s^{-2}. For the low-stability lower atmosphere, N^2 is ~4.37×10^{-7} s^{-2} and 3.42×10^{-6} s^{-2} for 11 LT and 16 LT, respectively.

The eddy diffusion is not well understood at low altitudes in the Venus atmosphere. Based on an analysis of Pioneer Venus radio occultation measurements, Woo and Ishimaru (1981) derived a value for the eddy diffusion of 4 m^2 s^{-1} near 60 km altitude. Bougher et al. (1986) found that values of eddy diffusion required in their model were smaller than values used in previous one-dimensional models. Upper limits to the eddy diffusivity were 500 m^2 s^{-1} for the dayside and about 1000 m^2 s^{-1} for the night-side. These values were applicable for altitudes above ~80 km. In their study of gravity wave propagation, Schubert and Walterscheid (1984) adopted a value of 4 m^2 s^{-1} and Young et al. (1987) adopted a constant value of 0.7 m^2 s^{-1} for the eddy diffusion. Based on a model relating breaking gravity waves to turbulent diffusion and using available measurements of turbulent diffusion coefficients at the planetary surface and at the homopause, Izakov (2001) derived a profile representing a lower bound to the eddy diffusivity. Values increased from 10^{-2} $m^2 s^{-1}$ at the surface, to 10^4 $m^2 s^{-1}$ at ~140 km altitude. Brecht et al. (2011) used values of eddy diffusivity that were a maximum of 1000 m^2 s^{-1} on the night-side and a constant value of 100 m^2 s^{-1} on the dayside. These profiles were applied above 80 km altitude, but no information was provided for lower altitudes (their model lower boundary was at 70 km altitude). Based on profiles of CO and CO_2 based on SOIR/Venus Express measurements, Mahieux et al. (2021) have determined values of eddy diffusivity in the upper troposphere and lower thermosphere. They determined that most previous studies substantially underestimated the values of eddy diffusivity in the 80–120 km height range. The value of eddy diffusivity at 140 km altitude was ~2×10^4 $m^2 s^{-1}$, in reasonable agreement with Izakov (2001).

Given the paucity of measurements in the middle and lower atmosphere, momentum eddy diffusivity ($\eta_e(z)$) profiles were devised that smoothly increased from small values in the lower atmosphere to larger values in the upper atmosphere. The model profile used is

$$\eta_e(z) = \eta_{LB} + 0.5\eta_{\max}\left\{1 + tanh\left[ln3\,\frac{(z - z_{mid})}{2H_\eta}\right]\right\} \quad (6)$$

where η_{LB} is the value of η at the lower boundary, $\eta_{\max}$ is the maximum (asymptotic) value of η at the upper boundary, z_{mid} is the altitude of inflection (which was held constant for all simulations), and H_η is a parameter that determines the gradient of η_e. We adopt four basic eddy diffusion profiles having the parameter values as shown in Table 1. The first profile (designated η_A) represents a nominal profile, while the second (η_B) is representative of that presented by Izakov (2001), as described above. The third (η_C) and fourth (η_D) profiles are representative of small and large diffusivities, respectively, and they are considered here to be extreme limits of the eddy diffusivity. The total viscosity profiles (molecular plus eddy) are shown in Fig. 4 along with values of the variable eddy diffusion profile taken from Table 1 of Mahieux et al. (2021). At 80 and 140 km altitude the values of eddy diffusivity based on profile D are factors of ~2.7 and ~ 3.8 smaller, respectively, than that of Mahieux et al. (2021). However, at intermediate altitudes the eddy diffusivity values associated with profile D are larger.

The eddy thermal conductivity was calculated from the eddy viscosity by assuming that the Prandtl number was equal to 0.1 (Schubert

Table 1
Eddy diffusion profiles and parameters used in Eq. (6) for this study.

Profile	η_{LB} (m^2 s^{-1})	$\eta_{\max}$ ($m^2 s^{-1}$)	H_η (km)	z_{mid} (km)
η_A	1	10^3	15	140
η_B	10^{-2}	10^4	9.56	140
η_C	10^{-3}	500	10	140
η_D	10	10^4	15	140

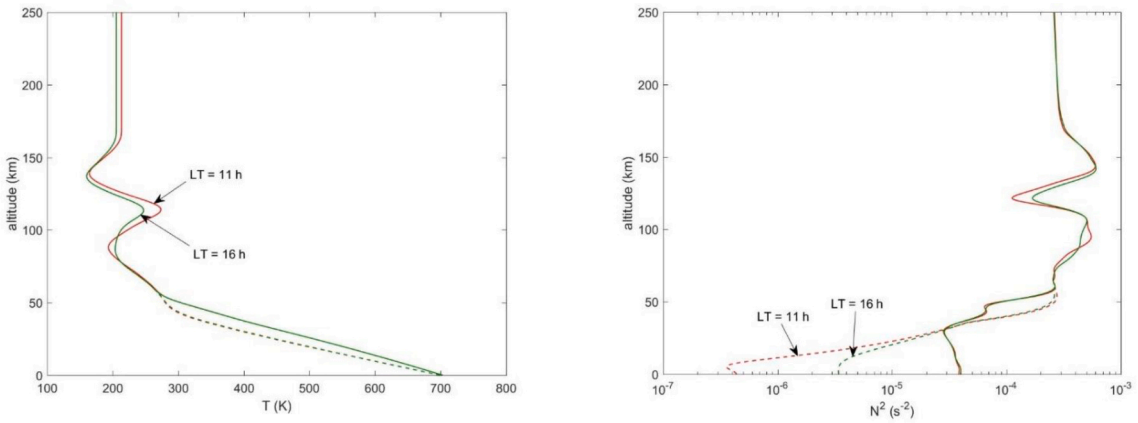

Fig. 3. Mean temperature (left panel) and the square of the Brunt-Vaisälä frequency (right panel) versus altitude for LT = 11 h (red curve) and LT = 16 h (green curve). Nominal (solid curves) and low-stability lower atmosphere (dashed curves) conditions are shown. (For interpretation of the references to colour in this figure legend, the reader is referred to the web version of this article.)

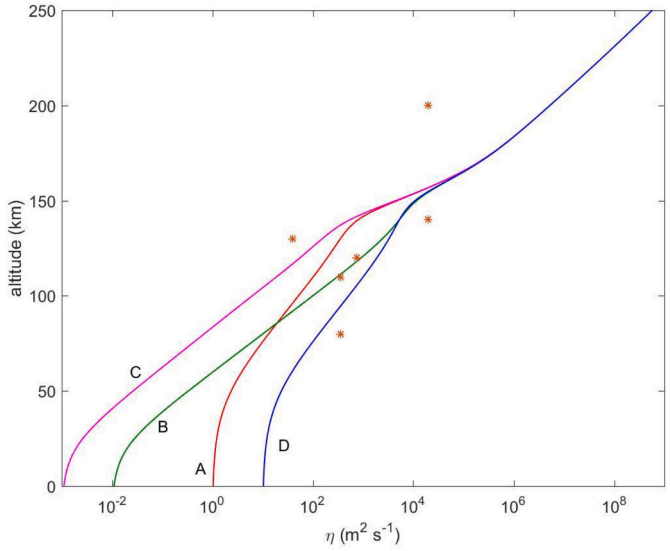

Fig. 4. The sum of the eddy and molecular viscosities. The parameters used in Eq. (6) to describe the four eddy viscosity profiles are provided in Table 1. At high altitudes where the molecular viscosity dominates all values are the same. The asterisks denote values of variable eddy diffusion taken from Table 1 of Mahieux et al. (2021).

et al., 1971). It has been suggested by Covey and Schubert (1981) that the eddy diffusion in the Venus atmosphere may not be isotropic. They proposed that the flatness of large-scale convection cells in the Venus clouds seen in UV images from Mariner 10 and Pioneer Venus spacecraft measurements can be explained by anisotropic eddy diffusion in which the horizontal eddy diffusivities are at least 10-fold greater than vertical diffusivities. We explored this possibility in which, following Covey and Schubert (1981), we set horizontal eddy diffusivities to be a factor of 10 or 100 larger than those given by Eq. (6). However, doing so had no significant impact on our results, and so our simulations performed here are based on isotropic eddy diffusivities as defined by Eq. (6).

At high altitudes (greater than ~80–90 km altitude) the wave amplitudes are apt to become quite large for certain combinations of mean state parameters, particularly those in the source region (lower atmospheric wind, eddy diffusivity and lower atmospheric stability). At these high altitudes, when the vertical gradients of the total (mean plus wave) potential temperature (θ) become negative, a wave will overturn, leading to mixing and enhanced diffusion (e.g., *Lindzen*, 1981; Walterscheid and Schubert, 1990). The enhanced eddy diffusion so produced acts to limit the wave to its saturation amplitude. We include a simplified version of this process in our model by incorporating a wave-induced eddy diffusion profile that extends over the region where $\partial\theta/\partial z$ is negative.

5. Results

Results are provided for single monochromatic waves as well as a full spectrum of waves defining our mountain waves. Given the number of parameters and the large parameter space to cover, to give a general view of the simulations we provide in Appendix C a table summarizing all of the figs.

5.1. Single wave model results

Before presenting the results of our simulations obtained with the spectral full-wave model, we use the single-wave version of this model in order to elucidate how the properties of the basic state impact the vertical propagation of discrete monochromatic gravity waves. The relevant atmospheric properties that impact the propagation of the waves are the eddy diffusivity, the vertical profile of the mean winds (through the local time), the low-altitude atmospheric stability and the lower boundary mean zonal wind. We primarily examine the vertical velocity amplitude, $|w'|$, as a function of altitude for three individual gravity waves having horizontal wavelengths λ_h of 100, 500 and 1000 km. The perturbations of horizontal velocity, u', and temperature, T', exhibit similar behavior to w' and because of this we do not present results for u' and we present only one set of results for T'. A local time of 11 h, a westward zonal wind of 1 m/s at the lower boundary, two different kinematic viscosity profiles (A and C), and the previously described two different temperature profiles (nominal and low-stability lower atmosphere) are considered.

In all cases shown in this section $|w'|$ is equal to 1 m/s at the lower boundary. Within a spectrum of waves, such as those considered in the section 5.2, the individual spectral amplitudes of w' are ~10^{-4} m/s at the lower boundary for the 500 km and 1000 km waves, and significantly smaller for the 100 km waves. Hence, the values obtained here for $|w'|$ and $|T'|$ are not meant to be realistic as they reach values exceeding 1 km/s and 1000 K, respectively. Instead, the results presented in this section merely serve the purpose of a first assessment of wave propagation in a qualitative rather than quantitative way.

Fig. 5 (left panel) is based on eddy viscosity profile A, which has a value of 1 m^2 s^{-1} at the lower boundary. The two sets of profiles are for the nominal stability/temperature profile (solid curves) and the low stability/temperature profile (dashed curves). Near the lower boundary the mean wind is small and therefore the waves are slow and have small vertical wavelengths. Based on the Scorer parameter provided in section 2, the minimum vertical wavelength at the lower boundary is ~0.56 km for the nominal-stability lower atmosphere. Hence, the waves are significantly dissipated just above the surface for propagation in the atmosphere having the nominal temperature profile (solid curves). Their amplitudes decrease rapidly away from the surface until the wind speed (and intrinsic phase speed of the waves) has increased sufficiently, which occurs just above 8 km altitude where $\overline{U}$ ~ 2 m/s. Above this height the wave amplitudes remain small, with some variations associated with strong partial reflections up to ~60 km altitude. Above this height the amplitudes increase with increasing height, reaching a maximum amplitude just below the critical level (at ~102.3 km altitude). The waves leak through the critical level and continue to propagate upward with significantly reduced amplitudes. This tunneling is facilitated by the presence of the viscosity, which removes the critical level singularity that would otherwise exist in its absence (Hazel, 1967). The approximate maintenance of wave amplitudes at altitudes above the critical level occurs due to the increasing mean wind speed (in the eastward direction). The waves attain a maximum amplitude at ~180 km altitude where the molecular kinematic viscosity has increased to ~10^6 m^2 s^{-1}, and amplitudes decrease at greater altitudes. The 100 km wave experiences less dissipation than the longer wavelength waves and experiences an amplitude growth between about 130 and 175 km altitude, with a decreasing amplitude at greater heights due to dissipation by molecular viscosity. The smaller dissipation rate for the wave of shorter horizontal wavelength can be understood following Young et al. (1994), but also applied here to the molecular viscosity. The ratio, r of the eddy diffusion term $\mu_e\partial^2 w'/\partial z^2$ (where $\mu_e = \overline{\rho}\eta_e$ is a coefficient of eddy viscosity) to the inertial term $\overline{\rho}Dw'/Dt$ in the linearized form of (1) for the vertical velocity component, can be shown to be approximately $r = \eta_e N^2/k\overline{U}^3$ (Young et al., 1994), where it has been assumed that the vertical variation of w' is purely sinusoidal. A larger value of r implies a larger damping of the wave. For a given value of η_e the damping will be larger for larger horizontal wavelength (smaller k), larger stability (N) and smaller wind speed ($\overline{U}$).

For propagation in the low-stability lower atmosphere (Fig. 5, left panel, dashed curves) the waves experience an amplitude growth at low altitudes. Despite the large eddy diffusivity, the relatively large vertical wavelengths near the surface (~ 9.5 km, based on the Scorer parameter)

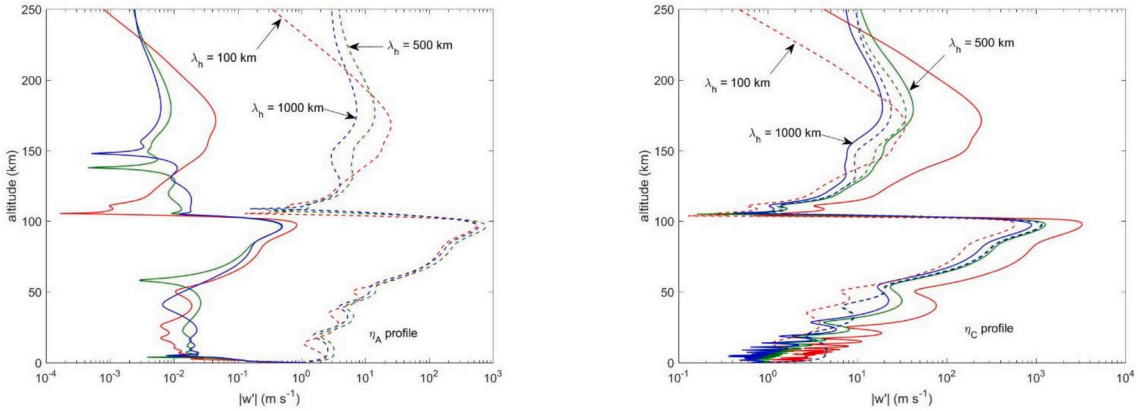

Fig. 5. Magnitude of the vertical velocity perturbation as a function of altitude for waves with horizontal wavelengths of 100 km (red curves), 500 km (green curves) and 1000 km (blue curves) propagating in the LT = 11 h mean state and for the nominal (A, left panel) and low (C, right panel) eddy diffusion profiles. Solid curves correspond to the nominal temperature profile while dashed curves correspond to the low-stability (smaller *N*) lower atmosphere temperature profile. The mean wind is – 1 m/s at the lower boundary. (For interpretation of the references to colour in this figure legend, the reader is referred to the web version of this article.)

mitigate the dissipation and the amplitudes grow with increasing height up to the critical level at ~103 km altitude. Partial reflections, as revealed by small undulations in wave amplitude over altitude, occur from the critical level. The resulting vertical structure between the surface and the critical level, exhibiting quasi nodes and antinodes, depends on the local intrinsic phase speed (i.e., $\overline{U}$), and hence exhibits shorter vertical wavelength variations at lower altitudes where $\overline{U}$ is smaller. The relative magnitude of these undulations is also smaller for wave propagation in the larger eddy diffusion environment (profile A), due to the weakening of the reflected downward propagating wave from the critical level. As previously noted, leakage through the critical level occurs. The overall wave structure is similar to that obtained for the stable lower atmosphere (solid curves) except that all wave amplitudes are larger by about three orders of magnitude.

The right panel of Fig. 5 shows the equivalent sets of results for eddy diffusivity profile C. Differences between the nominal and low-stability lower atmosphere cases are small. This is because the eddy diffusivity is small ($\sim 10^{-3}$ m^2 s^{-1}) near the lower boundary, and so the dissipation rate is small irrespective of differences in the vertical wavelengths associated with the different atmospheric stabilities. However, for the low-stability lower atmosphere (dashed curves) the wave amplitudes for eddy diffusivity profile C (right panel) are a factor of 3 to 4 times greater than those for eddy diffusivity profile A (left panel). Additionally, for the low-stability lower atmosphere, the reflections are more prominent for the case of diffusivity profile C than for profile A. This is because the smaller viscosity in the vicinity of the critical level associated with profile C causes the reflected waves to be stronger than they are for profile A.

We repeat the analysis for a local time of 16 h (see Fig. 6). As before, for the nominal-stability lower atmosphere the amplitudes at low altitudes are significantly more impacted by the larger values of eddy diffusivity associated with profile A (left panel) compared to those of profile C (right panel). For eddy diffusivity profile C (Fig. 6, right panel), differences in the wave amplitudes between the nominal-stability lower atmosphere (solid curves) and low-stability lower atmosphere (dashed curves) are relatively small. One of the most significant differences between the results shown in Fig. 6 and those shown in Fig. 5 is the absence of a critical level for LT = 16 h. Because of this, the wave amplitudes for altitudes greater than ~100 km are significantly greater than those for LT = 11 h. For LT = 16 h wave amplitudes can grow to large amplitudes in the thermosphere.

Other single-wave simulations (not shown) demonstrate that waves of short horizontal wavelength (~ 25 km or less) cannot propagate effectively to high altitudes under any conditions (local time, eddy diffusivity profile, wind at the lower boundary). For example, for extremely low eddy diffusivities (profile C) a wave of 25 km horizontal wavelength experiences a dramatic decrease in wave amplitude between the surface and about 50 km altitude, reduced by a factor of ~10^2 and

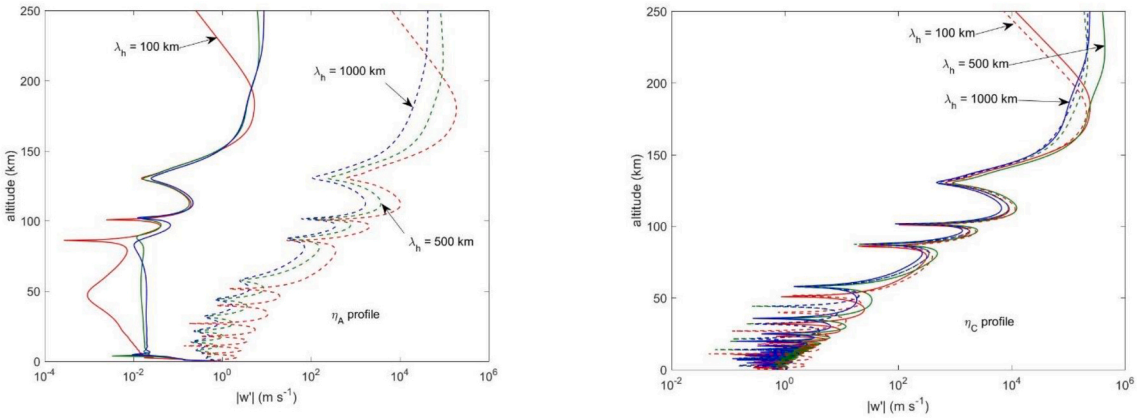

Fig. 6. Magnitude of the vertical velocity perturbation as a function of altitude for waves with horizontal wavelengths of 100 km (red curves), 500 km (green curves) and 1000 km (blue curves) propagating in the mean state at LT = 16 h and for the nominal (A, left panel) and low (C, right panel) eddy diffusion profiles. Solid curves correspond to the nominal temperature profile while dashed curves correspond to the low-stability (smaller *N*) lower atmosphere temperature profile. The mean wind is – 1 m/s at the lower boundary. (For interpretation of the references to colour in this figure legend, the reader is referred to the web version of this article.)

10^5 for the nominal and low static stability near-surface conditions, respectively. Such waves cannot make a significant contribution to the wave spectrum at higher altitudes under any circumstances.

In Fig. 7 we demonstrate the effect of including radiative damping on the altitude variation of the temperature and vertical velocity perturbations for a 500 km wavelength wave. The temperature perturbations (left panel) are impacted by the inclusion of the radiative damping only above about 120 km altitude, independent of the local time. In this case the amplitude decreases rapidly with increasing altitude when the CO_2 mixing ratios less than unity are not accounted for, while the decrease is less pronounced when the CO_2 mixing ratio is accounted for. In the latter case, most of the amplitude decrease due to the radiative damping occurs within about the first 30 km of its importance, that is, between ~120 km and 150 km altitude. At greater altitudes, the radiative damping becomes progressively smaller due to the reduced CO_2 mixing ratios above 150 km altitude, and the amplitude decreases at the same rate as it does in the absence of the radiative damping. With the inclusion of the radiative damping the temperature perturbation amplitude is reduced by a factor of ~2.5 by 160 km altitude.

The right panel of Fig. 7 shows the corresponding vertical velocity perturbation amplitudes. Because the radiative damping appears only in the energy equation, it directly impacts the temperature perturbations, whereas it indirectly impacts the vertical velocity perturbations. Thus, it has a greater impact on the magnitude of the temperature perturbations. As with the temperature perturbations, the effects of the radiative damping begin to become important by around 120 km altitude but diminish significantly by about 150 to 160 km altitude where the CO_2 mixing ratios becomes small. Due to the critical level filtering of the waves at LT = 11 h, the wave amplitudes have diminished to small, insignificant values at the altitudes where the radiative damping is effective. Hence, the radiative damping has a significant impact only on the LT = 16 h results.

5.2. 2-D model results

In this section we describe the simulations performed using our 2-D spectral full-wave model, which assumes a 1-D mountain shape. The Fourier solutions are computed within an ($n_x\Delta x$, $n_z\Delta z$) domain, with $\Delta x = 0.1a$ and $n_x = 1000$. For $a = 100$ km (see below) this equates to $\Delta x = 10$ km giving a Nyquist horizontal wavelength of 20 km. Experiments (not shown) have demonstrated that waves this short are strongly attenuated as they propagate vertically. In the vertical n_z was set to 15,000 for an upper boundary altitude of 350 km. Experimentation showed that this choice of spatial resolution produced convergent results.

In their discussion of VEGA balloon measurements, Young et al. (1987) noted that a feature of the vertical winds was an apparent zonal wavelength of ~500 km. Assuming a mountain width parameter a of 100 km in Eq. (5) leads to a vertical velocity spectrum $\widehat{w}(k,0)$ maximizing at a wavelength of ~540 km. Hence, $a = 100$ km is a reasonable parameter choice for our mountain, and we adopt this as the nominal value in our model. The impact of changing this value is discussed later.

We set the nominal mountain height h_0 to 1 km but as noted earlier the maximum value for linear waves is given by $(h_o)_{\max} = \overline{U}/N$. For the nominal-stability lower atmosphere, the resulting maximum height is ~0.32 km for $\overline{U} = 1$ m/s, irrespective of local time. For the low-stability lower atmosphere the corresponding maximum heights are ~3.8 km and 2.7 km for LT = 11 h and 16 h, respectively. We discuss the implications of the mountain height later in the discussion section. Based on Eq. (5), the maximum mountain slope for $a = 100$ km and $h_0 = 1$ km is ~0.007, which is one quarter of the slope of 0.028 adopted by Young et al. (1994).

The model provides the wave perturbations u', w' T' and p' as a function of horizontal position and height. We also calculate the potential temperature fluctuation θ' using

$$\theta' = \overline{\theta}\left(\frac{T'}{\overline{T}} - \kappa\frac{p'}{\overline{p}}\right) \tag{7}$$

where $\kappa = R/c_p$. When gravity wave amplitudes become large, they can exceed the stability threshold which occurs when the vertical gradient of the total potential temperature just becomes negative (e.g., Fritts, 1985, and references therein). Hence the requirement that a wave just becomes unstable is $d/dz(\overline{\theta} + \theta') = 0$. A useful alternative representation of this condition is that $S = (d\theta'/dz)/(d\overline{\theta}/dz) = -1$ and accordingly we use this ratio (S) to help interpret our results.

According to *Lindzen* (1981), a breaking wave generates just enough eddy diffusivity to offset the further growth of the wave. We add an additional eddy diffusivity in the vicinity of the large negative potential temperature gradients in order to mimic this process. We refer to this additional eddy diffusion profile as the wave-induced eddy diffusivity. This may be an underestimate of the eddy diffusivity required to limit wave growth, because unstable stratification is confined to a limited region of the wave, and the localization of turbulence requires either very large local eddy diffusivities or significant overturning (Walterscheid and Schubert, 1990). We prescribe an amount of eddy diffusion just

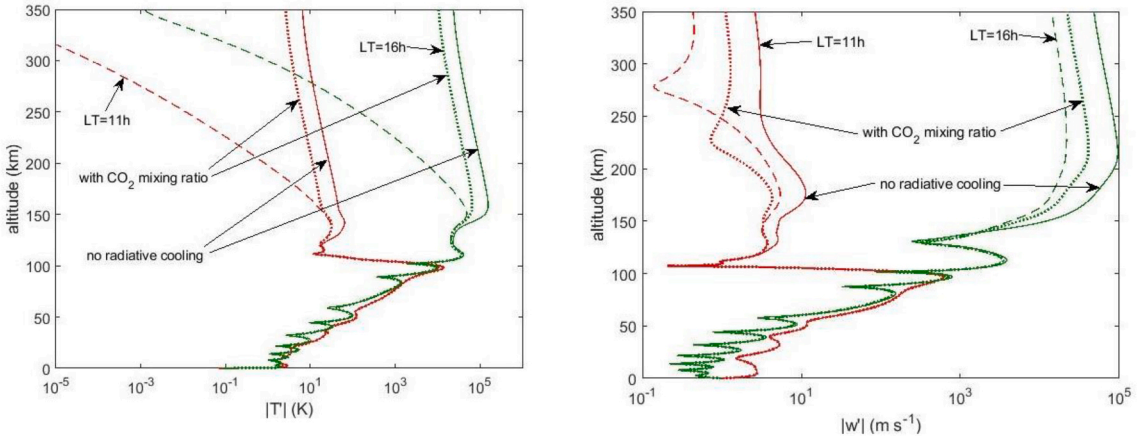

Fig. 7. Temperature perturbations (left panel) and vertical velocity perturbations (right panel) for a horizontal wavelength of 500 km for propagation in the low-stability lower atmosphere temperature profile and for the nominal eddy diffusion (profile A). Red and green curves correspond to LT = 11 h and 16 h, respectively. The mean surface wind is −1 m/s. Solid curves are for no radiative damping, dashed curves are for radiative damping assuming 100% CO_2, and the dotted curves correspond to radiative damping accounting for the altitude-dependent CO_2 mixing ratio. (For interpretation of the references to colour in this figure legend, the reader is referred to the web version of this article.)

large enough to maintain the wave at the limit of instability (i.e., $S_{min} = -1$). The parameters defining the wave-induced diffusivity profile are obtained by experimentation with the requirement that the additional wave-induced eddy diffusivity should have minimal impact on the wave at lower altitudes. This profile is modeled as a Gaussian function and the total eddy diffusion is then the sum of this profile and that of the eddy diffusivity profile prescribed by Eq. (6).

One of the main objectives of this paper is to compare the propagation of the mountain waves though the two different wind profiles discussed earlier, as shown in Fig. 2. The first, which is representative of the mean low latitude winds at LT = 11 h, displays a critical level near 100 km altitude which, as was discussed in the previous section, blocks the waves from entering the thermosphere. For the second wind profile, representative of the mean low latitude winds at LT = 16 h, there is no reversal of the mean zonal wind at any altitude and therefore the waves will not encounter a critical level during their upward propagation into the thermosphere. In the following two subsections we examine the characteristics of the wave propagation for these different wind profiles. We provide examples for which amplitudes grow to modest values in the upper atmosphere. A summary of these and other simulations is discussed further in the discussion section.

5.2.1. Spatial variation of the mountain waves

Below we present the variation of the density-weighted vertical velocity perturbation $\overline{\rho}^{1/2}w'$ with horizontal position and height. For the results shown, we have assumed a westward surface wind of 1 m/s, eddy diffusion profile A, and the low stability lower atmosphere. Results are shown for LT = 11 h and 16 h. The mountain is centered at a horizontal coordinate (longitude) of zero and extends to 400 km either side of that. The mountain wave is horizontally collocated with the mountain.

For LT = 11 h (left panel), the wave encounters a critical level near 100 km altitude, and so cannot propagate any higher. At altitudes between ~20 km and 90 km $\overline{\rho}^{1/2}w'$ is approximately conserved because the viscosity is relatively small. For LT = 16 h, there is no critical level, and the wave propagates into the thermosphere. In this latter case, the wave propagates upward into regions of ever-increasing viscosity and $\overline{\rho}^{1/2}w'$ begins to decrease with increasing height. In addition to amplitude information on Fig. 8, the sloping curves indicate the phase variation from which vertical wavelengths can be inferred. At low altitudes the vertical wavelength is larger for LT = 11 h (left panel) than it is for LT = 16 h (right panel), which is due to the smaller values of N at these altitudes for LT = 11 h (see Fig. 3b). At high altitudes, large mean winds and/or large viscosity leads to increased vertical wavelengths (e.g., right panel, altitudes greater than ~50 km).

In most of the remaining results we will present either the wave response as a function of height directly above the mountain center, or we will present the horizontally averaged response as a function of height. Doing so allows more information to be presented in a given figure.

5.2.2. Vertical wavelengths near the source

In this section we describe the effects of the eddy diffusivity, the stability of the lower atmosphere, and the magnitude of the surface wind on the vertical wavelength of the mountain waves for LT = 11 h. We consider surface winds of 1 m/s and 3 m/s, eddy diffusion profiles A (large diffusion) and C (low diffusion), and the nominal and low stability lower atmospheres. Although this range of parameters is somewhat limited, it serves the purpose of identifying how these parameters affect mountain wave propagation in the lower atmosphere. In later sections we consider a more complete range of parameters. In this section we present the wave response centered over the mountain.

Fig. 9 shows the variation of the density-weight vertical velocity perturbations, $\overline{\rho}^{1/2}w'$ over altitude from the surface to 30 km altitude. The vertical wavelength is smallest near the surface, and generally increases with increasing altitude as the wind speed increases. The smallest value of the near-surface vertical wavelength is ~1.4 km, and occurs for eddy profile C, nominal low-level stability, and a surface wind of 1 m/s (solid red curve). The corresponding vertical wavelength inferred from the Scorer parameter is about 1.4 km at ~4 km altitude. Decreasing the lower atmosphere stability from nominal to low values leads to a considerable increase in the vertical wavelength (red dashed curve). For the nominal stability lower atmosphere, increasing the surface wind from 1 m/s to 3 m/s leads to an approximate threefold increase in the vertical wavelength.

The green curves in Fig. 9 correspond to those cases based on eddy profile A, which has values at low altitudes that are ~100 times greater than those of eddy profile C. For the nominal low-level stability and a surface wind of 1 m/s (solid green curve) the vertical wavelength is ~4 km. This is larger than the corresponding case based on eddy profile C because dissipation has the effect of increasing the vertical wavelength of gravity waves (e.g, see Fig. 10 of Heale et al., 2014; Walterscheid and Hickey, 2011). Decreasing the lower atmosphere stability from nominal to low values leads to a considerable increase in the vertical wavelength (green dashed curve). For the nominal stability lower atmosphere, increasing the surface wind from 1 m/s to 3 m/s leads to a modest (~20%) increase in the vertical wavelength. The wave having the shortest vertical wavelength experiences the greatest dissipation, and consequently it has a considerably smaller amplitude than the other waves considered in Fig. 9. This case was for the nominal stability lower atmosphere, a 1 m/s surface wind, and for eddy diffusivity profile A (solid green curve). The wave experiencing the least dissipation had the largest

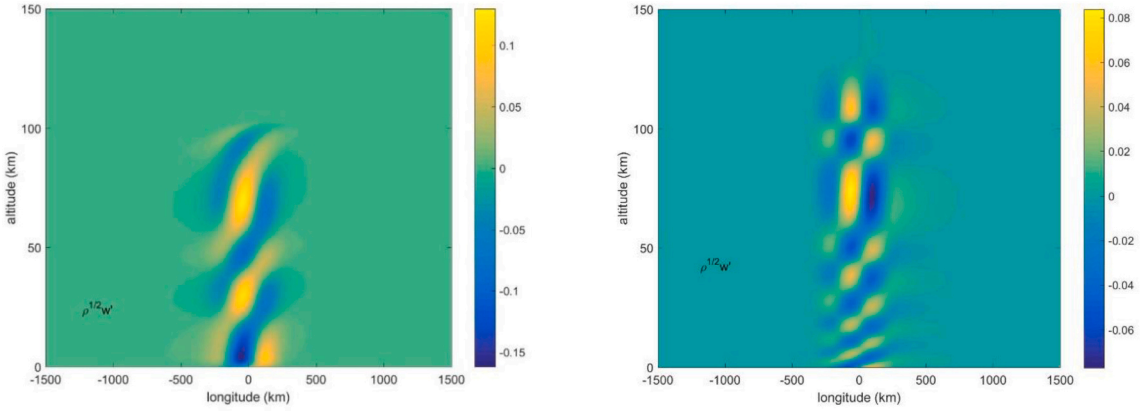

Fig. 8. The density-weighted vertical velocity perturbation ($\overline{\rho}^{1/2}w'$, in units of $kg^{1/2}\ m^{-1/2}\ s^{-1}$) for LT = 11 h (left panel) and LT = 16 h (right panel). In both cases the surface wind is 1 m/s, the eddy diffusivity is nominal (profile A), and the lower atmosphere stability is low. Below about 30 km altitude the vertical wavelength is much greater at LT = 11 h than at LT = 16 h due to the smaller values of N. Wave propagation above ~100 km is inhibited at LT = 11 h due to the critical level there.

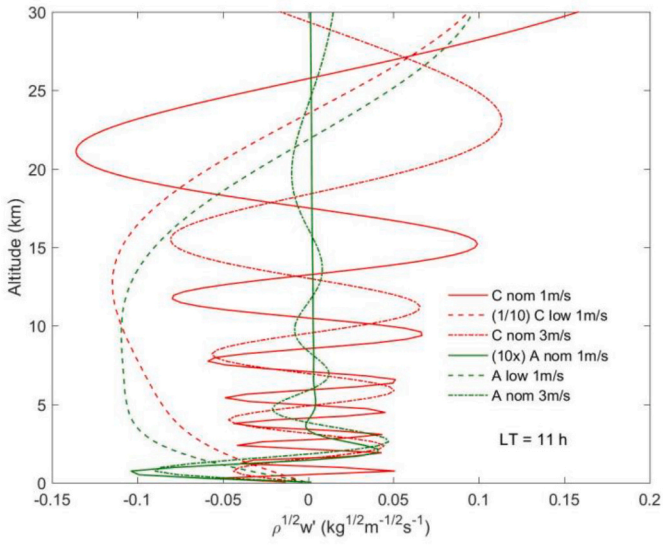

Fig. 9. The altitude variation of the density-weighted vertical velocity perturbation $\overline{\rho}^{1/2}w'$ at LT = 11 h calculated at the midpoint of the horizontal grid. The red and green curves are for low (C) and nominal (A), eddy diffusivity profiles, respectively. Solid curves are for nominal lower atmosphere stability and a surface wind of 1 m/s. The dashed curves correspond to the low stability lower atmosphere and a 1 m/s surface wind. The dashed-dotted curves correspond to the nominal lower atmosphere stability and a 3 m/s surface wind. For clarity, some of the results have been scaled by a factor of 10 (solid green curve) and one-tenth (dashed red curve). (For interpretation of the references to colour in this figure legend, the reader is referred to the web version of this article.)

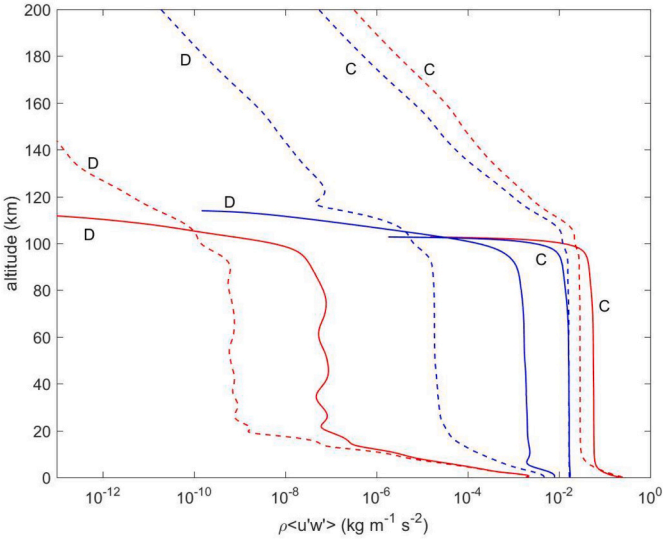

Fig. 10. Wave momentum fluxes versus altitude for a westward surface wind of 1 m/s. Solid and dashed curves are for LT = 11 h and LT = 16 h, respectively. Red and blue curves are for nominal and low stability of the lower atmosphere, respectively. Labels C and D denote low and high eddy diffusivities, respectively. All momentum fluxes for LT = 11 h (solid curves) exhibit a rapid reduction at heights above ~100 km due to the critical level there. (For interpretation of the references to colour in this figure legend, the reader is referred to the web version of this article.)

amplitude, which occurred for the low stability lower atmosphere, a 1 m/s surface wind, and for eddy diffusivity profile C.

The results shown in Fig. 9 demonstrate the sensitivity of the waves to the parameters of the lower atmosphere. Near the surface where wind speeds are typically small, the vertical wavelengths tend to be small in which case the waves may be significantly impacted by the near-surface eddy diffusivity. The exception to this is when the near-surface atmospheric stability is low and the corresponding vertical wavelengths are large. At altitudes well above the surface the mean winds increase considerably, which leads to increased vertical wavelengths and a reduction in the viscous dissipation. Hence, the variability in the state of the lower atmosphere, particularly the near-surface conditions, can have a dramatic impact on mountain wave propagation to higher altitudes.

5.2.3. *Wave momentum fluxes*

The wave momentum flux at a given altitude is defined as $\overline{\rho}\langle u'w'\rangle$, where all symbols are as previously defined, and where the angled brackets denote a horizontal average. The averaging was performed over a horizontal distance equal to twice the entire mountain width.

The wave momentum fluxes for LT = 11 h and LT = 16 h are shown in Fig. 10. In most cases they initially decrease with increasing height away from the surface where the wind speeds (and intrinsic phase speeds) are small, and the dissipation rates are comparatively large. The exception to this is for the case of low eddy diffusivity (η_C) and low stability in the lower atmosphere (large λ_z and low dissipation), for which the momentum flux is approximately constant at the lowest altitudes. At altitudes of 10–20 km above the surface where the wind speeds are larger and the viscous dissipation has decreased, the fluxes become approximately constant with increasing height. For a given combination of surface wind, eddy diffusivity and lower atmosphere stability, at low altitudes the fluxes are slightly larger for LT = 11 h than for LT = 16 h due to the larger low altitude mean winds in the former case (see Fig. 2). For LT = 11 h the waves experience a rapid decrease in the momentum fluxes just below 100 km altitude due to their critical level encounter. For LT = 16 h the waves do not encounter a critical level and propagate into the thermosphere, where viscous dissipation causes the momentum flux to decrease by several orders of magnitude between about 100 and 200 km altitude. The overall results clearly show that the fluxes can vary by many orders of magnitude based on the combination of surface wind, near-surface eddy diffusion, and near-surface atmospheric stability.

The results presented in Fig. 10 are for a limited subset of possible combinations of the relevant parameters (local time, eddy diffusivity, surface wind, and lower atmosphere stability). They show that once the waves reach an altitude of ~30 km, the momentum fluxes have become approximately constant, and that they remain so until the waves reach the upper atmosphere. Accordingly, we summarize the results using the complete set of combinations of relevant parameters by presenting the momentum fluxes at z ~ 30 km. These are shown in Tables S1a and S1b for LT = 11 h and 16 h, respectively.

5.2.4. *Comparison with observations*

In order to compare their simulation results with the observations of Fukuhara et al. (2017), Yamada et al. (2019) calculated a brightness-weighted temperature (for nadir viewing) defined as

$$T_W' = \int_{60km}^{80km} W(z)\,T'(z)\,dz \tag{8}$$

In Eq. (8) $W(z)$ represents the nominal weighting function of the Longwave Infrared Camera aboard the Akatsuki satellite, as described by *Taguchi* et al. (2007). It has a full-width at half-maximum value of ~10 km, and a central altitude of 65 km. We employ a weighting function having the same characteristics as theirs, but we have used 55 km for the lower range of integration. Also, the temperature perturbation T' used by Yamada et al. (2019) was a function of horizontal position (latitude and longitude) as well as altitude.

In order to compare our results with those of Fukuhara et al. (2017), we calculate T_W' as a function of longitude and present only the maximum value. It should be noted that because we are employing a 2-D

model we expect that derived wave amplitudes will be larger than those that would be obtained using a 3-D model. This is because our 2-D model does not account for any latitudinal spreading during the upward propagation of the wave packet, as simulations (Smith, 1980) and Venus observations (Fukuhara et al., 2017) show. Hence, our results should represent overestimates of the temperature fluctuation amplitudes. We do so for all combinations of relevant parameters (local time, eddy diffusivity, surface wind, and lower atmosphere stability). The results for local times of 11 h and 16 h are provided in Tables S2a and S2b, respectively. The modeled values of T_W' shown in these tables are similar to the ~2 K observed by Fukuhara et al. (2017) only for a limited range of conditions. Similarity to the observations tends to be favored for the low stability lower atmosphere for both local times considered. For LT = 11 h and the low stability lower atmosphere, surface wind speeds of 2–3 m/s give values of T_W' ranging from ~1.8–2.7 K across the four eddy diffusion profiles considered. For LT = 11 h and the nominal lower atmosphere stability, eddy diffusion profiles A and D lead to values of T_W' ranging from ~1.2–4.1 K across the different surface wind speeds considered. For LT = 11 h, the nominal stability lower atmosphere and eddy diffusion profiles B and C the calculated T_W' is not similar to the observed 2 K. For LT = 16 h the calculated values of T_W' are close to a value of 2 K only in a few instances: eddy profile A, low stability, surface wind of 1 m/s; eddy profile A, nominal stability, surface wind of 5 m/s; eddy profile D, low stability, and a surface wind of 2 m/s & 3 m/s).

Observations by Kitahara et al. (2019) of stationary wave features have revealed a dominant horizontal wavelength of ~510 km, which is comparable to the wavelength of 500 km inferred by Young et al. (1987) from VEGA balloon observations. Our results, based on the latter observations, provided a dominant horizontal wavelength of 500 km. However, the zonal wavelength of the waves reported by Fukuhara et al. (2017) was large (~ 1500 km) while the meridional extent of the disturbance was ~10,000 km. Further discussion of this and its relation to mountain width is provided in the Discussion section.

5.2.5. *Mean state accelerations*

The divergence of the wave momentum flux leads to a local acceleration of the mean state over the mountain. We denote this second-order acceleration $\partial\overline{U}_2/\partial t$, with

$$\frac{\partial \overline{U}_2}{\partial t} = -\frac{1}{\overline{\rho}}\frac{\partial}{\partial z}\overline{\rho}\langle u'w'\rangle \tag{9}$$

where $\langle u'w'\rangle$ is a second-order horizontal average of $u'w'$ and where all other symbols are as previously defined. The right side of Eq. (9) was calculated as a function of altitude and horizontal position and then averaged over a horizontal distance equal to twice the full mountain width.

The resulting accelerations for LT = 11 h and LT = 16 h are shown in Fig. 11. These results are based on a westward surface wind of 1 m/s, the nominal eddy diffusivity profile (A), and for the nominal lower atmosphere stability. There is no wave-induced diffusion included in these simulations because for this choice of mean state parameters the waves remain at small amplitudes throughout their upward propagation. This choice of lower atmosphere parameters also leads to the smallest mean state accelerations of all our simulations. For LT = 11, the forcing occurs over a fairly narrow region centered just below the critical level (near 102 km altitude). For LT = 16 h the wave propagates well into the thermosphere where they are dissipated by viscosity. In this case the forcing occurs over a broad region centered near 175 km altitude.

We have calculated the mean state forcing for different combinations of mean surface wind, eddy diffusivity profile and lower atmosphere stability and found that for a given local time (11 h or 16 h), and in the absence of wave-induced diffusion, the profile shape of the forcing as well as the altitude of the maximum forcing depends primarily on the mean wind profile and is approximately independent of the lower atmosphere parameters. (For LT = 11 h and for values of lower

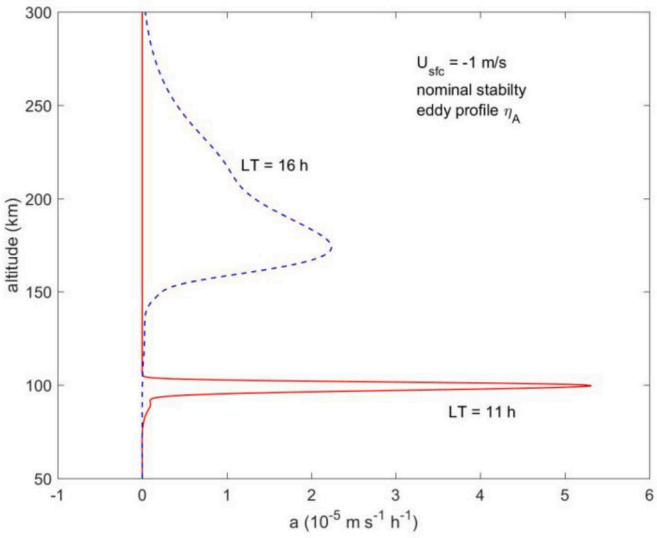

Fig. 11. Horizontally averaged mean state acceleration for LT = 11 h (solid red curve) and 16 h (dashed blue curve) and for a surface westward wind of 1 m/s, nominal eddy diffusivity (profile A), and for the nominal lower atmosphere stability. (For interpretation of the references to colour in this figure legend, the reader is referred to the web version of this article.)

atmosphere parameters for which amplitudes near the critical level do not remain small, the inclusion of wave-induced diffusion reduces the maximum forcing, and the profile is broadened over altitude.) However, for a given local time the magnitude of the forcing is strongly dependent on the specific combination of lower atmosphere parameters, and so this forcing depends critically on local time. We have tabulated the maximum forcing for the different combinations of lower atmosphere parameters in Table S3a (for LT = 11 h) and Table S3b (for LT = 16 h). The wave forcing in the vicinity of the critical level at LT = 11 h can be extremely large, even for those waves that are stable to convection. Examples of large forcing due to waves that are stable to convection can be seen in Table S3a (LT = 11 h) for the cases of a low stability lower atmosphere and for large eddy diffusivities (profile D), where the forcing increases from about 7 m/s/h to 39 m/s/h as the surface westward wind increases from 1 m/s to 5 m/s. Larger mean state forcing is possible for other combinations of parameters, but these occur for larger (nonlinear) wave amplitudes. One effect of the wave forcing on the mean state will be to cause the critical level to descend with time. To assess effects on the circulation one would have to evaluate zonally averaged values of wave drag/acceleration in terms of the global distribution of mountain wave sources. At this point all we can say is that given the large local values of acceleration global effects on the circulation could be important. The accelerations at LT = 11 h are representative of strong zonal westwards accelerations for local times earlier than 14 h, i.e. when there is a critical level centered near an altitude of 100 km. This zone is dominated by a transition from the westwards superrotation circulation to a Subsolar to Antisolar (SS-AAS) one. Therefore, a possible impact of mountain waves is to add an eastward component to the SS-AS circulation, especially, near in the vicinity of the SS point. This hypothesis cannot be caught by our model, but a time-dependent model (such a s a GCM), will be more suited to address this point.

For LT = 16 h the wave forcing is considerably greater than the LT = 11 h accelerations because of the considerably reduced atmospheric density at ~175 km altitude. We have not applied wave-induced diffusion for LT = 16 h because the wave amplitudes maximize at altitudes far above the turbopause (which is located at ~126–136 km, as discussed by Mahieux et al., 2021). More details of this are provided in the discussion section. Nevertheless, it is clear that the results for LT = 16 h suggest that the westwards component of the SS-AS is reduced, thus

contributing to make the eastward (evening) SS-AS branch stronger than the westward (morning) branch at altitudes above 150 km. However, quantifying this effect remains an open question, as explained in the discussion section.

5.2.6. Mean state heating and cooling

Dissipating gravity waves drive a downward potential sensible heat flux (Walterscheid, 1981; Schubert et al., 2003), causing cooling at high altitudes and heating at lower altitudes. Typically, the magnitude of the temperature decrease occurring at high altitudes is greater than the temperature increase occurring at lower altitudes because the former occurs in regions of lower atmospheric density (Walterscheid, 1981). The second order mean state heating (or cooling) rate, $\overline{Q}$, is related to the divergence of the sensible heat flux (Walterscheid, 1981) and the viscous flux of kinetic energy (Hickey et al., 2011) by

$$\overline{\rho} c_p \overline{Q} = -\frac{d}{dz}\left\{\overline{\rho} c_p \langle w' T' \rangle - \mu_m \frac{d}{dz}\left\langle \frac{1}{2} u'^2 \right\rangle\right\} \tag{10}$$

where all symbols are as previously defined. The first term in the parenthesis is the sensible heat flux, and the second term is the viscous flux of kinetic energy. Eq. (10) is valid when vertical derivatives of wave variables far exceed their horizontal derivatives. When that is not the case, the following equation applies (Schubert et al., 2003):

$$\overline{\rho} c_p \overline{Q} = \left\langle \vec{\sigma}_m' : \vec{\nabla}\, \vec{v}' \right\rangle - \frac{d}{dz}\left\{\overline{\rho} c_p \langle w' T' \rangle\right\} + \langle \vec{v}' \cdot \vec{\nabla} p' \rangle - \frac{d\overline{p}}{dz}\frac{\langle w' \rho' \rangle}{\overline{\rho}} \tag{11}$$

Here, the arrows denote vectors and the ":" sign represents the doubly-contracted product. We discovered that the viscous heating rate increased to unrealistically large values at high altitudes, and so it is not considered in these results. The reasons for the large values at high altitudes, seen in both our 2-D spectral results and also our single monochromatic wave results, are provided in the Discussion section. The right side of Eqs. (10) and (11) were calculated as a function of altitude and horizontal position and then averaged over a horizontal distance equal to twice the full mountain width.

In the previous section we found that the forcing of the mean state depended sensitively on the specific combination of lower atmosphere parameters used, with the smallest forcing occurring for a surface westward wind of 1 m/s, the nominal eddy diffusivity profile (A), and the nominal lower atmosphere stability. We adopt this same set of parameters here, and by so doing the resulting heating and cooling rates presented here are the smallest of all our simulations. It is important to note that values of heating and cooling rates for other combinations of the lower atmosphere parameters can be easily inferred by applying scaling factors derived from Tables S3a (for LT = 11 h) and S3b (for LT = 16 h), as discussed below.

The resulting heating and cooling rates associated with the sensible heat flux for LT = 11 h are shown in Fig. 12. These results are based on Eq. (10) (excluding viscous heating) which is approximately valid because the vertical derivatives are large in the vicinity of the critical level. There is no wave-induced diffusion included in these simulations because the wave amplitudes remain small throughout their upward propagation. The heating/cooling occurs over a fairly narrow region centered just below the critical level (near 102 km altitude). The profile shows cooling at the upper levels and heating below, as expected for the sensible heat flux (Walterscheid, 1981). The maximum heating rate is $\sim 8 \times 10^{-6}$ K/h and the maximum cooling rate is $\sim -1.75 \times 10^{-5}$ K/h.

For LT = 16 h the waves propagate well into the thermosphere where they are dissipated by viscosity. Because their vertical wavelengths become extremely large, Eq. (11) has been used to infer the heating/cooling rates, which are shown in the right panel of Fig. 12. The maximum heating and cooling rates occur near 150 km and 175 km altitude, respectively. The maximum heating rate is $\sim 2 \times 10^{-6}$ K/h and the maximum cooling rate is $\sim -3 \times 10^{-6}$ K/h.

As previously noted, these heating and cooling rates are the smallest obtained for all our simulations. They can serve as a reference value to derive heating and cooling rates for other combinations of parameters based on applying approximate scaling factors derived from the values of the mean state accelerations shown in Tables S3a and S3b. For the same parameters used to calculate the heating/cooling rates shown above, the maximum mean state acceleration for LT = 11 h shown in Table S3a is 5×10^{-5} m/s/h. The same table shows that the mean state acceleration for a 5 m/s westward surface wind, eddy diffusion profile D and a low stability lower atmosphere is 39 m/s/h, which is a factor of 7.8×10^5 larger. Hence, the maximum heating rate for this set of parameters will be a factor 7.8×10^5 larger than the heating rate of 8×10^{-6} K/h, that is, 6 K/h. Examination of Table S3a shows that heating and cooling rates much larger than this are possible for other combinations of lower atmosphere parameters (e.g., small values of eddy diffusivity in a nominal stability lower atmosphere).

A similar analysis is applied for LT = 16 h (using Table S3b), wherein for eddy diffusivity profile A and for a nominal stability lower atmosphere, the values of acceleration are 2.2×10^{-5}, 0.25, 169 and $> 10^5$ m/s/h for surface winds of −1, −2, −3 and − 5 m/s, respectively. Scaling the heating/cooling rates in the same way as before, we obtain maximum heating rates equal to 0.02, 15 and 9×10^3 K/h for surface winds of −2, −3 and − 5 m/s, respectively. The atmospheric flow is

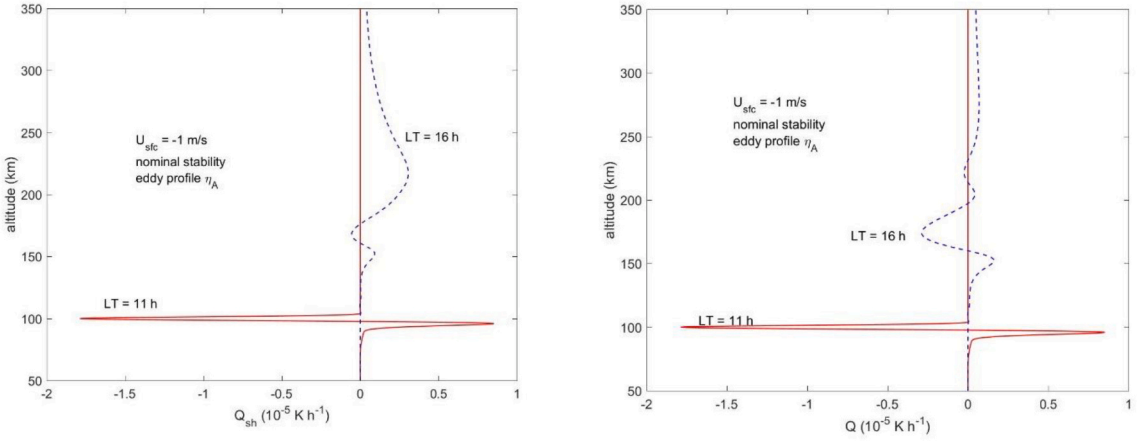

Fig. 12. Horizontally averaged mean state heating and cooling rates due to the sensible heat flux for LT = 11 h (solid red curves) and for a surface westward wind of 1 m/s, the nominal eddy diffusivity profile (A), and for the nominal lower atmosphere stability. The heating/cooling rates at LT = 16 h (dashed blue curves) in the left and right panels are based on Eqs. (10) and (11), respectively, with the viscous heating omitted. (For interpretation of the references to colour in this figure legend, the reader is referred to the web version of this article.)

strong and constant at these altitudes and will therefore transport momentum and heat efficiently away for the locations of wave forcing. However, the forcing will impact the zonal mean, in ways that we cannot model with our steady state model. These heating rates can be compared to contributions from the other main atmospheric processes. GCM simulations provide typical values of heating/cooling of order >50 K/h for processes such as UV/IR heating, CO_2 cooling, or conduction at altitudes above 100 km (Brecht and Bougher, 2012; Gilli et al., 2017). Therefore, in the most extreme surface conditions (e.g., extremely small eddy diffusivities or with surface winds ~5 m/s) the resulting heating rate from mountain waves may dominate the heating rates from other physical processes by at least one order of magnitude, and thus could substantially impact the upper atmospheric thermal structure and dynamics.

6. Discussion

Large mean state accelerations occurring near critical levels are not unexpected and have been noted before for terrestrial mountain waves. For example, using a linear spectral model Eckermann et al. (2016) found a peak acceleration of ~10^3 m/s h^{-1} occurring about 3 km below the critical level, with a density-weighted value of 350 m/s h^{-1} occurring over a height range of 4 km directly below the critical level. Here, we find that the mean state accelerations occurring at 11 UT in the vicinity of the critical level have peak values of 5 to 45 m/s h^{-1} for a surface wind of 1 m/s, for low stability in the lower atmosphere, and including wave-induced diffusion, with the larger values occurring for the smaller eddy diffusivities in the lower atmosphere. Wind speeds larger than 2 m/s produce waves having very large amplitudes below the critical level and consequently the forcing, which is proportional to the square of the amplitude, can become exceedingly large. As noted earlier, our 2-D model cannot account for any latitudinal spreading during upward propagation of the wave packet and hence our modeled amplitudes, fluxes and mean state forcing will be larger compared to those derived from a 3-D model.

We have compared our model results to observations in the region of the atmosphere just above the cloud tops. Our model provides temperature perturbation amplitudes similar to those observed for small surface winds of ~1 m/s, with values ranging from 0.5 K to ~3 K for large and small lower atmosphere eddy diffusivities, respectively. These values are similar to those observed from the Akatsuki satellite (Fukuhara et al., 2017). Increasing the surface wind increases the perturbation amplitudes at all altitudes. The vertical winds at these altitudes (not shown) are smaller than 0.5 m/s. Vertical winds measured over Aphrodite Terra from the VEGA balloon at altitudes near 55 km were 2–3 m/s (Young et al., 1987).

Based on UV imager observations obtained from Venus Express, Bertaux et al. (2016) found a correlation between the zonal winds at the cloud tops, and the elevation of the underlying topography. They inferred a deceleration of the zonal flow near the cloud tops of ~17 m/s per Venus day, which was assumed to be due to the breaking of small horizontal-wavelength gravity waves with a subsequent transfer of momentum to the mean state. The mesoscale modeling of Lefèvre et al. (2020), which included the effects of high-resolution topography, has inferred a deceleration of the zonal flow of ~3 m/s per Venus day at the cloud tops due to the resulting bow-shaped (stationary) waves. At an altitude of 67 km, our calculated accelerations (not shown) cover a wide range of values based on the combination of lower atmosphere parameters chosen. For example, for LT = 11 h, eddy diffusivity profile A, a low stability lower atmosphere and a surface westward wind of 2 m/s, the eastward acceleration is ~8.8 m/s per Venus day. For the same wave/conditions, the eastward acceleration in the vicinity of the critical level is considerably greater than this (23 m/s/h; see Table S3a). Hence, the impact of the waves on the mean state increases greatly with increasing altitude above the cloud tops.

Our model does not account for nonlinear effects associated with mountain heights exceeding the value $\overline{U}/N$, as discussed in section 3. However, as noted by Young et al. (1994), nonlinear effects should not propagate to heights well above the terrain. Additionally, these effects will be less important except for the highest terrain whenever the lower atmosphere has large lapse rates and low stability conditions. We adopted a nominal mountain height of 1 km for our simulations, and while this exceeded the limit noted above for the nominal-stability lower atmosphere simulations, it was within the linear regime for the low-stability lower atmosphere simulations.

Nonlinear effects associated with wave breaking may occur in the upper atmosphere whenever the total potential temperature gradient (wave plus mean) becomes negative. In addition to the mean state lapse rate, this condition depends on both the local amplitude and the vertical wavelength. In the case of LT = 11 h, the vertical wavelengths of the waves decrease appreciably as the critical level is approached. In those cases where the amplitude exceeded the nonlinear threshold (as inferred from the potential temperature gradient), we introduced a wave-induced eddy diffusivity to limit the wave amplitudes to their threshold value. This approach was based on *Lindzen* (1981), whereby breaking waves generate diffusion sufficient for them to saturate. For the case of LT = 16 h, where a critical level does not exist, the waves were able to propagate freely into the thermosphere where they attained large amplitudes. However, because their vertical wavelengths were also large, the gradients of potential temperature were typically small, and exceeded the nonlinear values only for the largest wave amplitudes. At these altitudes where the atmospheric density is extremely low it is unlikely that wave breaking of the form studied by *Lindzen* (1981) and others would occur. Accordingly, wave-induced diffusion was considered in only a few of the LT = 16 h cases, and it was never applied above ~145 km altitude (the approximate height of the turbopause). We found that when wave-induced diffusion was applied at lower thermospheric altitudes, the wave amplitudes would be reduced within the region of influence of the wave-induced diffusion, but they would quickly grow again above that region, with amplitudes increasing up to ~200 km altitude, and subsequently decreasing with a further increase of altitude. These large amplitude increases, which are due to the waves become quasi-evanescent at high altitudes and experiencing slow dissipation, occur despite the wave fluxes diminishing with increasing altitude (e.g., Fig. 8). This increase of wave amplitude with increasing altitude in the thermosphere has implications for the viscous heating rate per unit mass associated with the wave dissipation. We found that for LT = 16 h, the viscous heating rate increased with increasing altitude to unrealistically large values. This occurred in our 1-D simulations (monochromatic waves) as well as in our spectral (2-D) simulations and is a result of a combination of small wave dissipation (due to the extremely large vertical wavelengths the waves become quasi-evanescent) and low thermospheric mean densities (due to the small scale heights of ~13 km at high altitudes associated with a relatively cool thermosphere). We intend to perform a detailed study of this interesting phenomenon at a later time.

There is much uncertainty in the eddy diffusivity of the Venus atmosphere, both in its variation with position (for this study, altitude) and local time. The eddy diffusivities in the near-surface region, which are related to the lower atmosphere stability through vertical advection and mixing, are largely unknown. Our simulations demonstrate that the lower atmosphere eddy diffusivities and the lower atmosphere stability play a major role in the upward propagation of gravity waves from their mountain sources. Near the surface where the waves are slow the eddy diffusivity can significantly impact the wave amplitudes. For the largest eddy diffusivities considered wave amplitudes were small. The stability of the lower atmosphere impacts the ability of the waves to propagate away from the surface, with low stability conditions inhibiting the propagation of the waves (as noted for example by Young et al., 1987). We found that in general, the momentum fluxes were less sensitive to the eddy diffusivity for the lower stability lower atmosphere, particularly

for the larger surface wind speeds considered. This is because at low altitudes the vertical wavelengths are larger for the lower stability lower atmosphere and therefore the viscous dissipation (which is proportional to the vertical shear of the horizontal velocity perturbations) is smaller. For the smallest value of surface wind speed considered (1 m/s) the momentum flux reduced by a factor of ~10 as the eddy diffusivity increased from its minimum considered (profile C) to its maximum (profile D). For the nominal stability lower atmosphere, the corresponding decrease in the momentum flux was by a factor of $\sim 10^6$. This sensitivity of the momentum flux to the eddy diffusivity decreased as the surface wind speed increased.

Based on a spectral analysis of the low-latitude Venus topography spanning the Aphrodite Terra region (not shown) we used a value of $a = 100$ km in Eq. (11) describing our mountain shape, which leads to a maximum forcing for a horizontal wavelength of ~500 km. By considering the time delays between updrafts and downdrafts associated with vertical wind measurements from the VEGA-2 balloon, Young et al. (1987) deduced that wave disturbances had a zonal wavelength of ~500 km. A maximum forcing wavelength of 400 km was subsequently used in the study of Young et al. (1994). From observations of stationary waves Kitahara et al. (2019) deduced that the zonal wavelength was ~510 km, which closely agrees with the 500 km of Young et al. (1987). However, the simulations of Yamada et al. (2019) were based on a gaussian forcing function at the lower boundary having a full-width at half-maximum of approximately 880 km, which led to a wave disturbance at 65 km altitude having a zonal wavelength of ~1300 km and 1900 km on the eastern and western halves of their resultant wave packet, respectively. Their choice of characteristic spatial forcing led to good agreement with the bow wave observations of Fukuhara et al. (2017). We have experimented with other values of mountain width. Doubling the mountain width and also doubling the mountain height (to preserve the same mountain shape and slopes) gave the same vertical structure as the nominal mountain parameters, except that there was an overall slight reduction in wave amplitude. For a given mountain height, increasing the mountain width decreases the slopes and hence also decreases the vertical forcing. Our simulations presented here were based on a single value of the mountain width parameter $a = 100$ km in Eq. (11), which led to a maximum forcing at spectral wavelengths of ~540 km (as noted earlier in section 5.2). For a given mountain height, the slope (and therefore the spectral forcing amplitudes) would be reduced (increased) for wider (narrower) mountains. Based on Eq. (11), the maximum mountain slope for $a = 100$ km and $h_0 = 1$ km is ~0.007. This is about one quarter of the slope of 0.028 adopted by Young et al. (1994), which was based on a mountain height of 0.9 km and a horizontal wavelength of 200 km.

The wave forcing, described by Eq. (3), depends on the product of the surface wind speed and the mountain height. We have experimented with different combinations of these and found that the wind speed is more effective in generating larger amplitude waves at high altitudes. This is because an increase in mountain height increases all spectral components equally, but an increasing wind speed impacts the initial speed of the waves and allows them to propagate more easily in the lower atmosphere in the presence of eddy diffusion. We found that doubling the wind speed led to amplitudes at higher altitudes that were typically 20% greater than those associated with doubling the mountain height.

Sources of waves other than topographic forcing have not been considered here. Examples include convectively generated gravity waves (e.g., Baker et al., 2000), and waves generated through the obstacle effect mechanism (Lefèvre et al., 2018). Recent numerical simulations have shown that small scale ($\lambda \sim 250$ km) gravity waves can be spontaneously generated at the cloud top level by thermal tides (Sugimoto et al., 2021). The simulations revealed that this was more significant at low latitudes, where gravity waves decelerated the zonal winds where they were generated and propagated upward (to ~76–86 km altitude) where they accelerated the zonal flow. Hence, the gravity waves appeared to dissipate the thermal tide. Unlike the topographic forcing, other sources (such as convection) can produce small scale gravity waves. The recent radio occultation observations of Mori et al. (2021) have revealed short (0.5–4.0 km) vertical wavelength waves displaying just a few oscillations over altitude. These wave packets appeared to obey an m^{-3} power law (here m is the vertical wavenumber) which is indicative of saturating gravity waves, but it was concluded that the individual waves in the packets were not saturating. The earlier observations of Ando et al. (2015) had also discussed a saturated spectrum of gravity waves having vertical wavelengths shorter than about 5 km.

7. Conclusions

In this paper we have described a 2-D spectral full-wave model and used it to simulate the generation of mountain waves in the Venus atmosphere using an idealized mountain shape. The main objectives were to examine how the waves forcing and subsequent upward propagation depended on key surface parameters including the surface wind speed, the eddy diffusivity and the lower atmosphere stability. We also examined how the different propagation environments at high altitudes varied between two local times and the impact on the upward wave propagation of the waves into the thermosphere. The forcing of the mean state associated with wave dissipation was also presented for these high altitudes (~ 100 km and higher).

We have found that the lower atmosphere eddy diffusivity reduces the upward propagation of the waves, particularly when the surface winds are small and the lower atmosphere stability is nominal. For surface winds of 3 m/s or greater, and a low stability lower atmosphere the upward momentum flux in the lower atmosphere has a relatively small sensitivity to the eddy diffusivity. In this latter case, the vertical wavelengths are large, which strongly mitigates any effects of the eddy diffusivity. When the eddy diffusivity near the surface is extremely small, for any value of surface wind speed the vertical momentum fluxes are larger for the nominal stability lower atmosphere. The strong sensitivity to these parameters occurs because the wind speed (which equates to the intrinsic phase speed of the waves) is typically quite small near the surface. Waves having small vertical wavelengths near the surface are more susceptible to dissipation by eddy diffusivity, and those wavelengths are larger for the low stability lower atmosphere and also for faster surface wind speeds. We note that simulations (not shown) that included a non-zero vertical gradient of the mean wind at the lower boundary allowed the waves to achieve larger intrinsic phase speeds sooner as they propagated away from the surface, mitigating the low-altitude dissipation, and thereby leading to increased upward momentum fluxes compared to the zero mean wind gradient cases.

For a local time of 11 h (but more generally for local times of 09 LT to 14 LT) wave propagation into the thermosphere is inhibited by the presence of critical levels near 100 km altitude. As the waves approach the critical level their amplitudes grow and can become large enough for the waves to experience convective overturning, as suggested by the vertical gradient of the potential temperature. Strong forcing of the mean state also occurs, with the wave momentum deposition providing an acceleration opposing the mean wind in the vicinity of the critical

level. The divergence of the sensible heat flux leads to strong cooling of the atmosphere at the critical level and heating several kilometers below that.

As the mean wind evolves with time from LT = 11 h to LT = 16 h, the critical level near 100 km altitude disappears, providing easy access for the waves to the thermosphere. Propagating unimpeded, their amplitudes grow with increasing altitude up to 200–250 km. This growth occurs despite the increasing molecular kinematic viscosity because of the combination of large westward winds (equating to large intrinsic phase speeds) and small scale heights in the Venus thermosphere. Although wave amplitudes can become very large in the thermosphere, the total potential temperature gradient remains positive due to the extremely large vertical wavelengths of the waves, suggesting that the waves remain stable with respect to convection. Once in the thermosphere, the deposition of momentum due to these dissipating mountain waves will attempt to bring the mean winds to zero. The sensible heat flux leads to large heating and cooling rates in the thermosphere.

At a given local time, the maximum forcing of the mean state always occurs at an altitude determined primarily by the thermospheric mean winds and upper atmospheric viscosity. The surface conditions that determine the forcing (mountain parameters, surface mean wind, eddy diffusivity and static stability) play a minimal role in where these maxima occur, but they have a significant impact on their magnitudes. These results suggest that mountain waves may significantly impact the mean state at very high altitudes in the Venus atmosphere, both in terms of the momentum forcing and the thermal forcing. This forcing will depend sensitively on local time and also on near-surface conditions, but due to the slow rotation rate of Venus, conditions favoring strong forcing could extend for long periods of time. Forcing of this magnitude is not known to occur in the terrestrial atmosphere.

Declaration of Competing Interest

None.

Acknowledgments

TN and GS acknowledge NASA Akatsuki Participating Scientist Program support under grant 80NNSC20K1073. The authors thank the two anonymous reviewers whose constructive comments helped improve this paper.

Appendix A. Full-wave model equations

The linearized Navier-Stokes equations we use in Cartesian coordinates are (e.g., Hickey et al., 2000a)

$$\frac{\partial \rho'}{\partial t} + \vec{\overline{U}} \cdot \vec{\nabla}_h \rho' + \overline{\rho} \vec{\nabla} \cdot \vec{u}' + w' \frac{d\overline{\rho}}{dz} = 0 \tag{A1}$$

$$\overline{\rho} \frac{\partial \vec{u}'}{\partial t} + \overline{\rho} \vec{\overline{U}} \cdot \vec{\nabla}_h \vec{u}' + \vec{\nabla} p' - \vec{g} \rho' + \vec{\nabla} \cdot \vec{\sigma}' - \vec{\nabla} \cdot (\overline{\rho} \eta_e \vec{\nabla} \vec{u}') = -K_R \vec{u}' \tag{A2}$$

$$c_v \overline{\rho} \frac{\partial T'}{\partial t} + c_v \overline{\rho} \vec{\overline{U}} \cdot \vec{\nabla}_h T' + c_v \overline{\rho} w' \frac{d\overline{T}}{dz} - \overline{p} \vec{\nabla} \cdot \vec{u}' - \underset{\sim}{\nabla} \cdot (\kappa_m \vec{\nabla} T') - \frac{c_p \overline{T}}{\overline{\theta}} \vec{\nabla} \cdot (\overline{\rho} \kappa_e \vec{\nabla} \theta') = -r_{CO_2} K_N T' \tag{A3}$$

$$\frac{p'}{\overline{p}} = \frac{\rho'}{\overline{\rho}} + \frac{T'}{\overline{T}} \tag{A4}$$

$$\sigma'_{ij} = \mu_m \left(\frac{\partial u'_i}{\partial x_j} + \frac{\partial u'_j}{\partial x_i} - \frac{2}{3} \delta_{ij} \vec{\nabla} \cdot \vec{u}' \right) \tag{A5}$$

These are the linearized equations of mass continuity, momentum conservation, energy conservation, the ideal gas equation of state, and the viscous stress tensor, respectively. An overbar denotes the basic undisturbed mean state, which is assumed to vary only in the vertical direction, z, while tildes and double lines appearing below symbols indicate vectors and tensors, respectively. Primes denote linear perturbations about the mean. Also, $\vec{g}$ is the gravitational acceleration, p is pressure, ρ is mass density, T is temperature, and $\vec{u}$ is the velocity with components u and w in the x (eastward) and z directions, respectively. The variable θ appearing in (A3) is the potential temperature, defined as $\theta = T(p_{00}/p)^{R/c_p}$, where p_{00} is a reference pressure, R is the gas constant, and where c_p and c_v are the specific heats at constant pressure and volume, respectively. The molecular dynamic viscosity is μ_m, the coefficient of thermal conductivity is κ_m, and the eddy momentum and thermal diffusivities are η_e and κ_e, respectively. The Rayleigh friction coefficient is K_R. The effects of radiative damping are included with a coefficient$K_N$multiplied by the CO_2 mixing ratio (r_{CO_2}), as described later in this section. Also, $\vec{\nabla}_h$ is the horizontal component of the gradient vector. The steady mean wind, denoted by upper case letters, is assumed to be in the horizontal, zonal direction only ($\vec{\overline{U}} = \overline{U}\hat{i}$).

The vertically propagating plane monochromatic waves in t, and x are of the form $A_j(z) \exp i(\omega t - kx)$ where ω is the wave frequency, and k is the horizontal components of the wavenumber vector in the x direction. The complex wave amplitude isA_j, where the subscript refers to each of the perturbation velocity components, pressure and temperature. The lower boundary is at the ground ($z = 0$) and the upper boundary is nominally at a height z = 350 km. At the lower boundary waves are forced in the vertical velocity. At the upper boundary, a radiation condition is applied, but instead of defining the vertical wavenumber using the dispersion relation of *Hickey and Cole* (1987), as has usually been the case with this model, we instead define it using a viscosity wave solution as described in more detail in the Appendix B. This solution is more appropriate when the upper boundary is at very high altitudes where the kinematic viscosity is extremely large.

Radiative damping, arising from the emission of 15 μm radiation from CO_2, is employed based on the findings of Crisp (1989). The radiative damping of Crisp (1989) has been previously used for tidal simulations by Takagi and Matsuda (2005), for planetary wave simulations by Kashimura et al. (2019), and for gravity wave simulations by Hinson and Jenkins (1995) and Yamada et al. (2019). As in these prior studies we assume that the relaxation time decreases exponentially from 10^4 Earth days at the surface to 0.1 Earth days at 120 km altitude. We extend this to higher altitudes than the previous studies by assuming that it decreases exponentially above 120 km altitude with a constant scale height of ~10.5 km (equal to that at 120 km altitude). The inverse of the radiative relaxation time is defined as K_N (see Eq. (A3)). Up to ~120 km altitude CO_2 is the major constituent, but its mixing ratio decreases above that height. To account for the effect of this decrease on the radiative damping, for altitudes greater than 120 km we multiply K_N by the CO_2 mixing ratio (r_{CO2}), as indicated in Eq. (A3).

Crisp (1989) also accounted for the scale-dependence of the radiative damping and concluded that the radiative damping rates for vertical scale sizes of ~7 km and 30 km would be a factor of approximately 5.0 and 1.4 times greater, respectively, than the nominal (infinite vertical wavelength) radiative damping rate. Accordingly, we include this scale dependence in our computations, with the appropriate factor being determined by the approximate vertical wavelength provided by the Scorer parameter. We use the damping rate appropriate for the ~7 km vertical scale for LT = 11 h simulations because the vertical wavelengths assume small values in the vicinity of the critical level. Based on the results of single-wave simulations for a horizontal wavelength of 500 km, for LT = 16 h we use the damping rate appropriate for an ~30 km vertical scale.

Appendix B. Full-wave model upper boundary conditions

In the thermosphere the molecular kinematic viscosity increases exponentially with increasing altitude. At high thermospheric altitudes the molecular kinematic viscosity attains values large enough to significantly dissipate the wave causing a reduction in the wave vertical energy flux with increasing altitude. At even greater altitudes the rapid diffusion tends to eliminate vertical phase gradients so that the vertical wavelength becomes exceedingly large (e.g., *Hickey and Cole*, 1987 and references therein) and the waves become quasi-evanescent. At these altitudes the vertical transport of wave energy is dominated by the effects of viscosity while the contribution due to the work done by the pressure forces becomes insignificant (Walterscheid and Hickey, 2011). At these heights the wave heating is due almost entirely to the divergence of the viscous flux of kinetic energy (Hickey et al., 2011). Because of the exceedingly large vertical wavelengths, the viscous wave dissipation (which acts on the velocity gradients) approaches zero. This leads to the imaginary part of the vertical wavenumber also approaching small values and the wave amplitudes do not in general decrease with increasing altitude.

Under these conditions just described, with extreme values of kinematic viscosity in the upper region of our model, the waves behave more as viscosity waves than as internal gravity waves. Hence, when we apply the radiation condition at the upper boundary of our model, rather than solving our dispersion equation for the vertical wavenumber m_{GW} that includes viscosity and thermal conductivity (*Hickey and Cole*, 1987), we instead assume a viscous wave solution. It is important to note that we do this only when the upper boundary is placed at an extremely high altitude, which in this case is 350 km. If the upper boundary were placed at a lower altitude, such as 250 km, we would not assume a viscosity wave solution for the radiation condition but would instead apply the usual gravity wave radiation condition. We also note that choosing the appropriate root of the cubic gravity wave dispersion equation (in $m^2{}_{GW}$) becomes more difficult at high altitudes where the kinematic viscosity is extremely high. A detailed discussion of the issues associated with identifying the appropriate gravity wave root of the dispersion equation is provided by Knight et al. (2019).

The equation describing a viscosity wave is (e.g., *Hickey and Cole*, 1987, and references therein)

$$3\widehat{\eta}\widehat{R} = \beta \tag{B1}$$

where $\beta = \Omega^2/gHk^2$, $\widehat{\eta} = i\Omega\mu_m/3\overline{p}$ and where

$$\widehat{R} = \frac{1}{k^2}\left\{k^2 + m^2 + \frac{1}{4H^2} - \frac{im}{2H}\right\} \tag{B2}$$

All other terms are as previously defined in Appendix A. For $m^2 \ll k^2$ and setting $\Omega = -k\overline{U}$ for mountain waves, (B1) and (B2) lead to the vertical wavenumber at the upper boundary, m_{UB}, defined as

$$m_{UB} = \frac{-2kH\overline{U}}{\eta} - 2iH\left(k^2 + \frac{1}{4H^2}\right) \tag{B3}$$

Eq. (B3) shows that the vertical wavelength, $2\pi/\,\mathrm{Re}\,(m_{UB})$, is proportional to the product of the kinematic viscosity and the horizontal wavelength. For waves with large horizontal wavelengths λ_h such that the second term in the parentheses dominates (that is, $\lambda_h \gg 4\pi H$), then $\mathrm{Im}(m_{UB}) \approx -1/2H$. This term exactly offsets the usual $e^{z/2H}$ growth that gravity waves experience in the absence of dissipation, and therefore the wave amplitudes remain approximately constant with increasing altitude at great heights. More typical gravity waves, for which λ_h does not satisfy this condition, will experience a decreasing amplitude with increasing height. Using (B3) at the upper boundary instead of the more usual m_{GW} based on the gravity wave dispersion equation provides a more robust solution for the upper radiation condition at very high altitudes. This is because, as previously stated, when the gradients become exceedingly small the viscous damping and resulting imaginary part of the vertical wavenumber approach zero and wave amplitudes will not decrease with increasing altitude. Knight et al. (2019) have also noted that the imaginary part of the vertical wavenumbers of the dissipative modes (comprising the viscosity and thermal conduction waves) are larger than those of the gravity waves, meaning that the former experience a more rapid amplitude decrease with increasing altitude than do gravity waves.

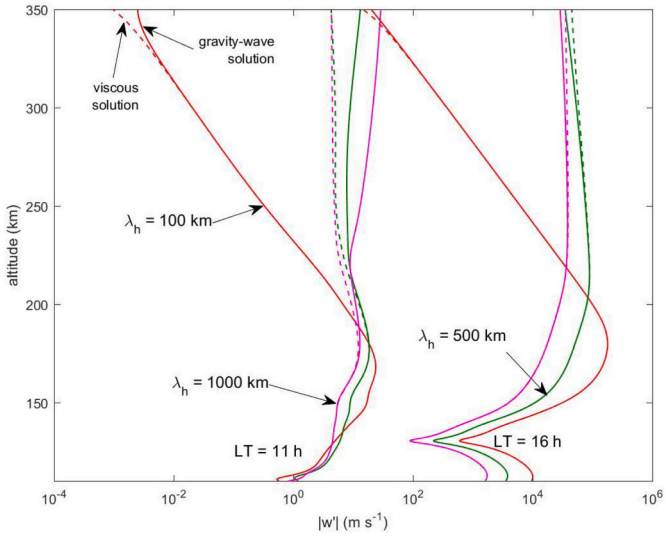

Fig. B1. *Vertical velocity amplitude versus altitude for the low stability lower atmosphere, LT = 11 h and 16 h, and for λ_h = 100, 500 and 1000 km. The upper boundary condition is based on either the gravity wave dispersion equation (solid curves) or the viscosity wave solution (dashed curves). The curves are colored red, green and violet for horizontal wavelengths of 100 km, 500 km and 1000 km, respectively. (For interpretation of the references to colour in this figure legend, the reader is referred to the web version of this article.)*

Fig. B1 shows altitude profiles of the vertical velocity amplitudes obtained for three different values of horizontal wavelength (λ_h = 100, 500 and 1000 km) and for two local times (LT = 11 h and 16 h) based on using either the dispersion relation of *Hickey and Cole* (1987) or Eq. (B3) to evaluate the radiation condition at the upper boundary. At high altitudes the use of the two different upper boundary conditions usually led to similar results except for the case when the longest wavelength (λ_h = 1000 km). In this case the dispersion equation of *Hickey and Cole* (1987) led to an unrealistic increase of $|w'|$ with increasing altitude above about 220 km, whereas the use of Eq.(B3) led to $|w'|$ approaching a constant value at high altitudes.

Appendix C

In order to present a general view of the simulations, below we provide an additional table summarizing all the figures based on the following nomenclature:

u1_LT11_eA_w500_ls means lower boundary wind of −1 m/s, LT = 11H, eddy diffusion profile A; wavelength 500 km; low stability, etc. …

Figure	Case
5a	u1_LT11_eA_ns_w100; u1_LT11_eA_ns_w500; u1_LT11_eA_ns_w1000; u1_LT11_eA_ls_w100; u1_LT11_eA_ls_w500; u1_LT11_eA_ls_w1000;
5b	u1_LT11_eC_ns_w100; u1_LT11_eC_ns_w500; u1_LT11_eC_ns_w1000; u1_LT11_eC_ls_w100; u1_LT11_eC_ls_w500; u1_LT11_eC_ls_w1000;
6a	u1_LT16_eA_ns_w100; u1_LT16_eA_ns_w500; u1_LT16_eA_ns_w1000; u1_LT16_eA_ls_w100; u1_LT16_eA_ls_w500; u1_LT16_eA_ls_w1000;
6b	u1_LT16_eC_ns_w100; u1_LT16_eC_ns_w500; u1_LT16_eC_ns_w1000; u1_LT16_eC_ls_w100; u1_LT16_eC_ls_w500; u1_LT16_eC_ls_w1000;
7a; 7b	u1_LT11_eA_ls_w500_nodamp; u1_LT11_eA_ls_w500_100CO2; u1_LT11_eA_ls_w500_varCO2; u1_LT16_eA_ls_w500_nodamp; u1_LT16_eA_ls_w500_100CO2; u1_LT16_eA_ls_w500_varCO2;
8a	u1_LT11_eA_ls
8b	u1_LT16_eA_ls
9	u1_LT11_eA_ls; u1_LT11_eA_ns u3_LT11_eA_ns; u1_LT11_eC_ls; u1_LT11_eC_ns u3_LT11_eC_ns;
10	u1_LT11_eC_ls; u1_LT11_eC_ns; u1_LT11_eD_ls; u1_LT11_eD_ns; u1_LT16_eC_ls; u1_LT16_eC_ns; u1_LT16_eD_ls; u1_LT16_eD_ns;
11; 12; 13	u1_LT11_eA_ns; u1_LT16_eA_ns

Appendix D. Supplementary data

Supplementary data to this article can be found online at https://doi.org/10.1016/j.icarus.2022.114922.

References

Ando, H., Imamura, T., Tsuda, T., Tellman, S., Patzold, M., Häusler, B., 2015. Vertical wavenumber spectra of gravity waves in the Venus atmosphere obtained from *Venus express* radio occultation data: evidence for saturation. J. Atmos. Sci. 72, 2318–2329.

Baker, R.D., Schubert, G., Jones, P.W., 2000. Convectively generated internal gravity waves in the lower atmosphere of Venus: II. Mean wind shear and wave-mean flow interaction. J. Atmos. Sci. 57, 200–215. https://doi.org/10.1175/1520-0469(2000)057<0200:CGIWI>2.0.CO;2.

Bertaux, J.-L., Khatuntsev, I.V., Hauchecorne, A., Markiewicz, W.J., Marcq, E., Lebonnoise, S., Patsaeva, M., Turin, A., Fedorova, A., 2016. Influence of Venus topography on the zonal wind and UV albedo at cloud top level: the role of stationary gravity waves. J. Geophys. Res. Planets 121, 1087–1101. https://doi.org/10.1002/2015JE004958.

Blamont, J.E., Young, R.E., Seiff, A., Ragent, B., Sagdeev, R., Linkin, V.M., Preston, R.A., 1986. Implications of the VEGA balloon results for Venus atmospheric dynamics. Science 231 (4744), 1422–1425.

Bougher, S.W., Dickinson, R.E., Ridley, E.C., Roble, R.G., Nagy, A.F., Cravens, T.E., 1986. Venus mesosphere and thermosphere. II. Global circulation, temperature and density variations. Icarus 68, 284–312.

Brecht, A.S., Bougher, S.W., 2012. Dayside thermal structure of Venus' upper atmosphere characterized by a global model. J. Geophys. Res. 117 (E8).

Brecht, A.S., Bougher, S.W., Gerard, J.-C., Parkinson, C.D., Rafkin, S., Foster, B., 2011. Understanding the variability of nightside temperature, NO UV and O_2 IR nightglow emissions in the Venus upper atmosphere. J. Geophys. Res. 116, E08004. https://doi.org/10.1029/2010JE003770.

Covey, C.C., Schubert, G., 1981. Mesoscale convection in the clouds of Venus. Nature 290, 17–20.

Crisp, D., 1989. Radiative forcing of the Venus atmosphere: II. Thermal fluxes, cooling rates, and radiative equilibrium temperatures. Icarus 77, 391–413.

Durran, D., June 1990. Mountain waves and downslope winds. In: Atmospheric Processes over Complex Terrain. Meteorological Monographs, vol. 23. American Meteorological Society, pp. 59–83. No.45.

Durran, D., 2003. In: Holton, J.R., Pyle, J., Curry, J.A. (Eds.), Lee Waves and Mountain Waves, in *Encyclopedia of Atmospheric Sciences*. Elsevier Sciences Ltd., pp. 1161–1169

Eckermann, S., et al., 2016. Dynamics of orographic gravity waves observed in the mesosphere over the Auckland Islands during the deep propagating gravity wave experiment (DEEPWAVE). J. Atmos. Sci. 73, 3855–3876. https://doi.org/10.1175/JAS-D-16-0059.1.

Fukuhara, et al., 2017. Large stationary gravity wave in the atmosphere of Venus. Nat. Geosci. 10, 85–88.

Gilli, G., Lebonnois, S., González-Galindo, F., López-Valverde, M.A., Stolzenbach, A., Lefèvre, F., Lott, F., 2017. Thermal structure of the upper atmosphere of Venus simulated by a ground-to-thermosphere GCM. Icarus 281, 55–72.

Gilli, G., Navarro, T., Lebonnois, S., Quirino, D., Silva, V., Stolzenbach, A., Schubert, G., 2021. Venus upper atmosphere revealed by a GCM: II. Model validation with temperature and density measurements. Icarus 366, 114432.

Heale, C.J., Snively, J.B., Hickey, M.P., Ali, C.J., 2014. Thermospheric dissipation of upward propagating gravity wave packets. J. Geophys. Res. Space Physics 119, 3857–3872. https://doi.org/10.1002/2013JA019387.

Hickey, M.P., Walterscheid, R.L., Schubert, G., 2000a. Gravity wave heating and cooling in Jupiter's thermosphere. Icarus 148, 266–281.

Hickey, M.P., Walterscheid, R.L., Richard, P.G., 2000b. Secular variations of atomic oxygen in the mesopause region induced by transient gravity wave packets. Geophys. Res. Lett. 27, 3599–3602.

Hickey, M.P., Schubert, G., Walterscheid, R.L., 2009. Propagation of tsunami-driven gravity waves into the thermosphere and ionosphere. J. Geophys. Res. 114, A08304. https://doi.org/10.1029/2009JA014105.

Hickey, M.P., Schubert, G., Walterscheid, R.L., 2011. Gravity Wave Heating and Cooling of the Thermosphere: Sensible Heat Flux and Viscous Flux of Kinetic Energy, vol. 116, p. A12326. https://doi.org/10.1029/2011JA016792.

Hinson, D.P., Jenkins, J.M., 1995. Magellan radio occultation measurements of atmospheric waves on Venus. Icarus 114, 310–327.

Huber, M.L., Harvey, A.H., 2011. Thermal conductivity of gases. In: CRC Handbook of Chemistry and Physics, 92nd ed. CRC-Press, Boca Raton, FL.

Izakov, M.N., 2001. Turbulence and anomalous heat fluxes in the atmospheres of Mars and Venus. Planet. Space Sci. 49, 47–58.

Kashimura, H., et al., 2019. Planetary-scale streak structure reproduced in high-resolution simulations of the Venus atmosphere with a low-stability layer. Nat. Commun. 10, 23. https://doi.org/10.1038/s41467-018-07919.

Kitahara, T., Imamura, T., Sato, T.M., Yamazaki, A., Lee, Y.J., Yamada, M., et al., 2019. Stationary features at the cloud top of Venus observed by ultraviolet imager onboard Akatsuki. J. Geophys. Res. 124 https://doi.org/10.1029/2018JE005842.

Knight, H.K., Broutman, D., Eckermann, S.D., 2019. A causality-preserving Fourier method for gravity waves in a viscous, thermally diffusive, and vertically varying atmosphere. Wave Motion 88, 226–256.

Kouyama, T., Imamura, T., Taguchi, M., Fukuhara, T., Sato, T.M., Yamazaki, A., Nakamura, M., 2017. Topographical and local time dependence of large stationary gravity waves observed at the cloud top of Venus. Geophys. Res. Lett. 44, 12,098–12,105. https://doi.org/10.1002/2017GL075792.

Lebonnois, S., Schubert, G., 2017. The deep atmosphere of Venus and the possible role of density-driven separation of CO_2 and N_2. Nat. Geosci. 10, 473–477.

Lefèvre, M., Spiga, A., Lebonnois, S., 2020. Mesoscale modeling of Venus' bow-shape waves. Icarus 335, 113376.

Mahieux, A., Yelle, R.V., Yoshida, N., Robert, S., Piccialli, A., Nakagawa, H., Kasaba, Y., Mills, F.P., Vandaele, A.C., 2021. Determination of the Venus eddy diffusion profile from CO and CO2 profiles using SOIR/Venus express observations. Icarus 361, 114388.

Mori, R., Imamura, T., Ando, H., Hausler, B., Patzold, M., Tellmann, S., 2021. Gravity wave packets in the Venusian atmosphere observed by radio occulatation experiments: comparison with saturation theory. J. Geophys. Res. 126, e2021JE006912 https://doi.org/10.1029/2021JE006912.

Navarro, T., Schubert, G., Lebonnois, S., 2018. Atmospheric mountain wave generation on Venus and its influence on the solid planet's rotation rate. Nat. Geosci. 11 (7), 487–491. https://doi.org/10.1038/s41561-018-0157-x.

Navarro, T., Gilli, G., Schubert, G., Lebonnois, S., Lefèvre, F., Quirino, D., 2021. Venus' upper atmosphere revealed by a GCM: I. structure and variability of the circulation. Icarus 366, 114400.

Peralta, J., Hueso, R., Sanchez-Lavega, A., Lee, J.Y., Garcia-Munoz, A., Kouyama, T., Sagawa, H., Sato, T.M., Piccioni, G., Tellmann, S., Imamura, T., Satoh, T., 2017. Stationary waves and slowly moving features in the night upper clouds of Venus. Nat. Astr. 1, 1–5.

Reinecke, P.A., Durran, D., 2009. The overamplification of gravity waves in numerical solutions to flow over topography. Mon. Weather Rev. 137, 1533–1549.

Schubert, G., Walterscheid, R.L., 1984. Propagation of small-scale acoustic-gravity waves in the Venus atmosphere. J. Atmos. Sci. 41, 1202–1213.

Schubert, G., Young, R.E., Hinch, J., 1971. Prograde and retrograde motion in a fluid layer: consequences for thermal diffusion in the Venus atmosphere. J. Geophys. Res. 76, 2126–2130.

Schubert, G., Hickey, M.P., Walterscheid, R.L., 2003. Heating of Jupiter's thermosphere by the dissipation of upward propagating acoustic waves. Icarus 163, 398–413.

Smith, R.B., 1980. Linear theory of stratified hydrostatic flow past an isolated mountain. Tellus 32, 348–364.

Sugimoto, N., Fujisawa, Y., Kashimura, H., Noguchi, K., Kuroda, T., Takagi, M., Hayashi, Y.-Y., 2021. Generation of gravity waves from thermal tides in the Venus atmosphere. Nature. Communications 12, 3682. https://doi.org/10.1038/s41467-021-24002-1.

Takagi, M., Matsuda, Y., 2005. Sensitivity of thermal tides in the Venus atmosphere to basic zonal flow and Newtonian cooling. Geophys. Res. Lett. 12, L02203. https://doi.org/10.1029/2004GL022060.

Walterscheid, R.L., 1981. Dynamical cooling induced by dissipating internal gravity waves. Geophys. Res. Lett. 8 (12), 1235–1238. https://doi.org/10.1029/GL008i012p01235.

Walterscheid, R.L., Hickey, M.P., 2011. Group velocity and energy flux in the thermosphere: limits on the validity of group velocity in a viscous atmosphere. J. Geophys. Res. 116, D12101. https://doi.org/10.1029/2010JD014987.

Walterscheid, R.L., Schubert, G., 1990. Nonlinear evolution of an upward propagating gravity wave: overturning, convection, transience and turbulence. J. Atmos. Sci. 47, 101–125.

Woo, R., Ishimaru, 1981. Eddy diffusion coefficient for the atmosphere of Venus from radio scintillation measurements. Nature 289, 383–384.

Yamada, T., Imamura, T., Fukuhara, T., Taguchi, M., 2019. Influence of the cloud-level neutral layer on the vertical propagation of topographically generated gravity waves on Venus. Earth Planets Space 71, 123–130. https://doi.org/10.1186/s40623-019-1106-7.

Young, R.E., Walterscheid, R.L., Schubert, G., Seiff, A., Linkin, V.M., Lipatov, A.N., 1987. Characteristics of gravity waves generated by surface topography on Venus: comparison with the VEGA balloon results. J. Atmos. Sci. 44, 2628–2639.

Young, R.E., Walterscheid, R.L., Schubert, G., Pfister, L., Houben, H., Bindschadler, D.L., 1994. Characteristics of finite amplitude stationary gravity waves in the atmosphere of Venus. J. Atmos. Sci. 51, 1857–1875.